

**EXPERIMENTAL AND THEORETICAL ROTORDYNAMIC COEFFICIENTS
AND LEAKAGE OF STRAIGHT SMOOTH ANNULAR GAS SEALS**

A Thesis

by

BRADLEY GRAY KERR

Submitted to the Office of Graduate Studies of
Texas A&M University
in partial fulfillment of the requirements for the degree of

MASTER OF SCIENCE

December 2004

Major Subject: Mechanical Engineering

**EXPERIMENTAL AND THEORETICAL ROTORDYNAMIC COEFFICIENTS
AND LEAKAGE OF STRAIGHT SMOOTH ANNULAR GAS SEALS**

A Thesis

by

BRADLEY GRAY KERR

Submitted to Texas A&M University
in partial fulfillment of the requirements
for the degree of

MASTER OF SCIENCE

Approved as to style and content by:

Dara W. Childs
(Chair of Committee)

Paul G.A. Cizmas
(Member)

John M. Vance
(Member)

Dennis O'Neal
(Head of Department)

December 2004

Major Subject: Mechanical Engineering

ABSTRACT

Experimental and Theoretical Rotordynamic Coefficients and
Leakage of Straight Smooth Annular Gas Seals. (December 2004)

Bradley Gray Kerr, B.S., University of Arkansas

Chair of Advisory Committee: Dr. Dara W. Childs

Results are presented for experimental and theoretical rotordynamic coefficients and leakage of straight smooth annular gas seals. Experimental rotordynamic coefficients were measured and trends in changes of rotordynamic coefficients with operating variables such as rotor speed, back-pressure, fluid preswirl, and seal clearance are analyzed.

Experimental results show that cross-coupled stiffness coefficients are highly influenced by fluid preswirl and only moderately influenced by other operating parameters, whereas direct damping is nearly unaffected by changes in operating parameters. Effective damping, a good indicator of stability, is highly affected by fluid preswirl. Although rotordynamic coefficients of straight smooth annular gas seals are assumed to be frequency independent, experimental results suggest a frequency dependent nature at high back-pressures and high excitation frequencies.

Experimental results for rotordynamic coefficients and leakage are compared with theoretical predictions of ISOTSEAL, an isothermal-flow, two-control-volume, bulk-flow rotordynamic analysis program. All rotordynamic coefficients are under-predicted. Direct stiffness is poorly predicted while cross-coupled stiffness and direct

damping are predicted reasonably well. Leakage is also consistently under-predicted.

Theory predicts a slight frequency dependent nature for a limited number of test configurations.

ACKNOWLEDGMENTS

I would like to thank my parents for accepting nothing less than my best and always believing in me. Thank you mom for your boundless love, support, and encouragement. Thank you dad for encouraging me to pursue my dreams. Thank you to the many family members and friends that have supported and encouraged me. Thank you to Charles and Gina Ivey for the opportunity to work, learn, and develop many life skills.

Thank you to the many educators who have touched my life throughout my education. You have taught me more than just academics. I would like to especially thank Dr. Dara Childs for the opportunity to work and learn at the Turbomachinery Laboratory.

TABLE OF CONTENTS

	Page
ABSTRACT	iii
ACKNOWLEDGMENTS	v
TABLE OF CONTENTS	vi
LIST OF FIGURES	viii
LIST OF TABLES	xi
NOMENCLATURE	xii
INTRODUCTION	1
Literature Review	3
Description of the Test Rig	5
Fluid Preswirl	8
Seal Leakage	9
Calculation of Rotordynamic Coefficients	10
Test Conditions	13
Test Data Uncertainty	15
EXPERIMENTAL RESULTS	17
Direct Stiffness	18
Cross-Coupled Stiffness	21
Direct Damping	24
Effective Stiffness	26
Effective Damping	26
EXPERIMENT VERSUS PREDICTIONS	30
Direct Stiffness	31
Cross-Coupled Stiffness	36
Direct Damping	40
Effective Stiffness	44
Effective Damping	44
Seal Leakage	49
SUMMARY	52

	Page
REFERENCES	54
APPENDIX A	56
APPENDIX B	60
VITA	63

LIST OF FIGURES

Figure	Page
1 Smooth Seal Rotor Assembly with Fluid Preswirl	1
2 Forces on a Forward Precessing Rotor	2
3 Cross Sectional View of Test Apparatus	6
4 Cross Section of Stator Housing	7
5 Cross Section of Fluid Preswirl Rings	8
6 Typical Elements of the Frequency-Response Function	12
7 Non-Dimensional Direct Stiffness vs. Excitation Frequency, C _r = 0.2mm	20
8 Non-Dimensional Direct Stiffness vs. Excitation Frequency, Zero Preswirl, C _r = 0.1mm	20
9 Non-Dimensional Cross-Coupled Stiffness vs. Excitation Frequency, C _r = 0.2mm	22
10 Non-Dimensional Cross-Coupled Stiffness vs. Excitation Frequency, Zero Preswirl, C _r = 0.1mm	23
11 Normalized Direct Damping vs. Excitation Frequency, C _r = 0.2mm	25
12 Normalized Direct Damping vs. Excitation Frequency, Zero Preswirl, C _r = 0.1mm	26
13 Normalized Effective Damping vs. Excitation Frequency, C _r = 0.2mm	28
14 Normalized Effective Damping vs. Excitation Frequency, Zero Preswirl, C _r = 0.1mm	29
15 Experimental and Theoretical Direct Stiffness vs. Excitation Frequency, Zero Preswirl, C _r = 0.2mm	33

Figure	Page
16 Experimental and Theoretical Direct Stiffness vs. Excitation Frequency, Medium Preswirl, $C_r = 0.2\text{mm}$	34
17 Experimental and Theoretical Direct Stiffness vs. Excitation Frequency, High Preswirl, $C_r = 0.2\text{mm}$	35
18 Experimental and Theoretical Direct Stiffness vs. Excitation Frequency, Zero Preswirl, $C_r = 0.1\text{mm}$	36
19 Experimental and Theoretical Cross-Coupled Stiffness vs. Excitation Frequency, Zero Preswirl, $C_r = 0.2\text{mm}$	37
20 Experimental and Theoretical Cross-Coupled Stiffness vs. Excitation Frequency, Medium Preswirl, $C_r = 0.2\text{mm}$	38
21 Experimental and Theoretical Cross-Coupled Stiffness vs. Excitation Frequency, High Preswirl, $C_r = 0.2\text{mm}$	39
22 Experimental and Theoretical Cross-Coupled Stiffness vs. Excitation Frequency, Zero Preswirl, $C_r = 0.1\text{mm}$	40
23 Experimental and Theoretical Direct Damping vs. Excitation Frequency, Zero Preswirl, $C_r = 0.2\text{mm}$	41
24 Experimental and Theoretical Direct Damping vs. Excitation Frequency, Medium Preswirl, $C_r = 0.2\text{mm}$	42
25 Experimental and Theoretical Direct Damping vs. Excitation Frequency, High Preswirl, $C_r = 0.2\text{mm}$	43
26 Experimental and Theoretical Direct Damping vs. Excitation Frequency, Zero Preswirl, $C_r = 0.1\text{mm}$	44
27 Experimental and Theoretical Effective Damping vs. Excitation Frequency, Zero Preswirl, $C_r = 0.2\text{mm}$	46
28 Experimental and Theoretical Effective Damping vs. Excitation Frequency, Medium Preswirl, $C_r = 0.2\text{mm}$	47
29 Experimental and Theoretical Effective Damping vs. Excitation Frequency, High Preswirl, $C_r = 0.2\text{mm}$	48

Figure	Page
30 Experimental and Theoretical Effective Damping vs. Excitation Frequency, Zero Preswirl, $C_r = 0.1\text{mm}$	49
31 Experimental and Theoretical Leakage vs. Preswirl Ratio, $C_r = 0.2\text{mm}$	51
1A Stator Model with Radial Stiffeners.....	58

LIST OF TABLES

Table	Page
1 Seal Dimensions	13
2 Test Conditions	14
3 Uncertainty of Measured Parameters	16
4 Variables Used for Non-dimensional and Normalized Stiffness and Damping.....	17
1A Baseline Data	56
2A Baseline Data with Radial Stiffeners	57

NOMENCLATURE

A_{ij}	Stator acceleration [L/T ²]
A_x, A_y	Fourier transformed components of stator acceleration [L/T ²]
C	Direct damping [FT/L]
C^*	Normalized direct damping [T]
c	Cross-coupled damping [FT/L]
C_{eff}	Effective damping [FT/L]
C^*_{eff}	Normalized effective damping [T]
C_r	Radial clearance [L]
D_r	Rotor diameter [L]
D_s	Seal diameter [L]
D_x, D_y	Fourier transformed components of x, y [L]
F_x, F_y	Fourier transformed components of f_x and f_y [F]
f	Friction factor
f_x, f_y	Stator excitation input force component [F]
f_{xg}, f_{yg}	Annular gas seal reaction force components [F]
g	Acceleration due to gravity [L/T ²]
H_{ij}	Frequency-response-function [F/L]
H_w	Inches of water [L]
$Im()$	Imaginary part of a function
j	$\sqrt{-1}$
K	Direct stiffness [F/L]
K^*	Non-dimensional direct stiffness
k	Cross-coupled stiffness [F/L]
k^*	Non-dimensional cross-coupled stiffness
K_{eff}	Effective direct stiffness [F/L]
K^*_{eff}	Non-dimensional effective direct stiffness
L	Seal length [L]
M	Inertia coefficient [M]
M_s	Stator mass [M]
m	Blasius friction factor index
N	Rpm [1/T]
n	Blasius friction factor coefficient
P	Pressure [F/L ²]
P_{in}	Inlet pressure [F/L ²]
R_c	Gas constant [FL/(MT)]
Re	Reynolds number
$Re()$	Real part of a function
T_{in}	Temperature [K]
v_t	Inlet tangential (swirl) velocity [L/T]
x, y	Relative displacement between stator and rotor [L]
\dot{x}, \dot{y}	Relative velocity between stator and rotor [L/T]

\ddot{x}, \ddot{y}	Relative acceleration between stator and rotor [L/T^2]
ΔP	Differential pressure [F/L^2]
ε	Precession amplitude [L]
\dot{m}	Mass flow rate [M/T]
ρ_a	Density of air [M/L^3]
ρ_w	Density of water [M/L^3]
φ	Non-dimensional flow coefficient
ω	Rotor speed [1/T]
Ω	Excitation frequency [1/T]

Subscripts

ij	Direction of response and force
------	---------------------------------

INTRODUCTION

Annular gas seals are used in a variety of turbomachinery applications. Different seal configurations have been developed to address leakage and stability problems experienced in the operation of turbomachines. Each seal configuration has its own set of rotordynamic and leakage characteristics. Common applications of annular seals include steam turbines, high-pressure compressors, turbo-pumps, and other applications where a fluid is compressed or expanded in a series of stages. The particular seal of interest here is the smooth annular gas seal. Smooth annular seals are generally used as floating seals whereby the seal stator is self-centering when the turbomachine is in operation.

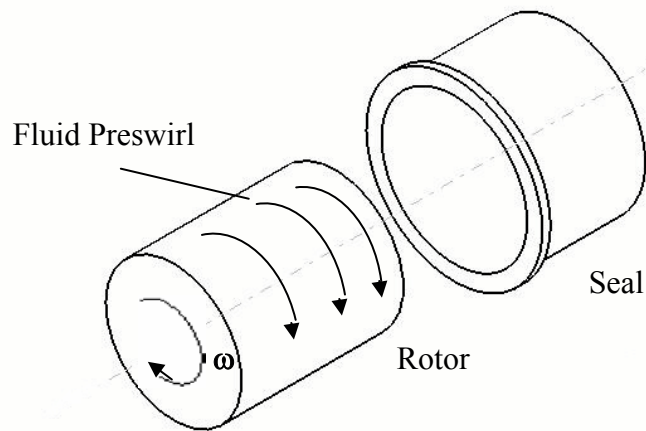


Fig. 1 Smooth Seal Rotor Assembly with Fluid Preswirl

Figure 1 shows a smooth seal stator and smooth rotor combination. This is a simplified representation of what was tested. A model for the reaction forces generated by the smooth seals is given by:

$$-\begin{Bmatrix} f_{xg} \\ f_{yg} \end{Bmatrix} = \begin{bmatrix} K & k \\ -k & K \end{bmatrix} \begin{Bmatrix} x \\ y \end{Bmatrix} + \begin{bmatrix} C & c \\ -c & C \end{bmatrix} \begin{Bmatrix} \dot{x} \\ \dot{y} \end{Bmatrix} + M \begin{Bmatrix} \ddot{x} \\ \ddot{y} \end{Bmatrix}, \quad (1)$$

where K and C are the direct stiffness and direct damping of the system. The cross-coupled stiffness and damping are represented by k and c . All rotordynamic coefficients of smooth seals are assumed frequency independent.

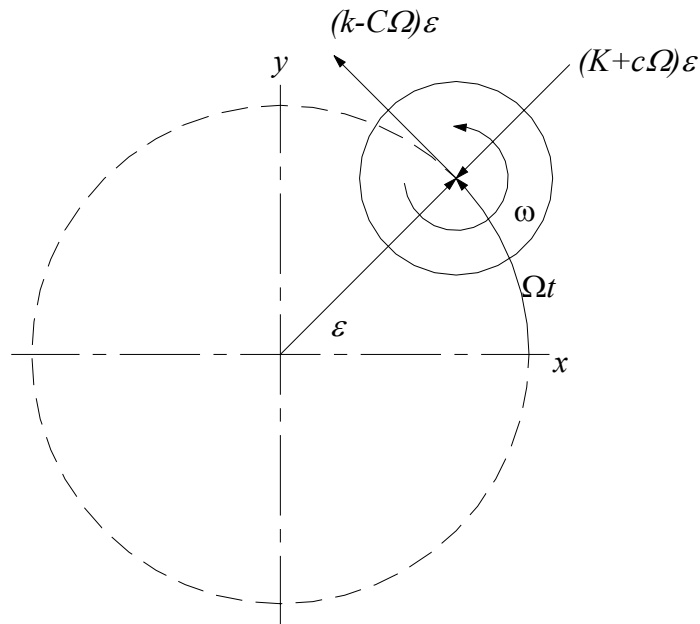


Fig. 2 Forces on a Forward Precessing Rotor

Figure 2 shows the forces acting on a forward precessing rotor. The radial force developed by K and c act to center the rotor and does not have much influence on the

stability of the system. The tangential force developed by C and k is a follower force and greatly influences the stability of the system.

Literature Review

Fleming [1-3] contributed the initial analysis of smooth annular gas seals. The analysis presented a method to calculate the radial stiffness of annular gas seals. Fleming notes that with the straight smooth annular gas seal negative stiffness sometimes occurs, an undesirable situation. Fleming [2] later expanded his work to include calculations for damping. However, his work did not include the circumferential velocity component of the fluid flow resulting in a one-dimensional analysis. Without the inclusion of the circumferential velocity component of flow, the cross-coupled coefficients cannot be determined.

Nelson [4, 5] developed a method of obtaining all the rotordynamic coefficients of equation (1). Additionally, he notes the effects of fluid pre-rotation and choked flow on the rotordynamic coefficients. His solution technique is similar to Childs [6, 7], whereby a set of governing equations based on Hirs' [8] turbulent bulk flow model are developed, and then a perturbation analysis is employed to obtain a set of zero- and first-order equations. Integration of the zeroth-order equations yields the leakage and integration of the first-order equations yields the direct and cross-coupled coefficients. Nelson et al. [9] discuss predicted and experimental rotordynamic coefficients of constant-clearance and convergent-tapered seals. Results of Nelson et al. [9] verify the predictions by Nelson [4, 5] and Fleming [2, 3], that an optimally tapered seal will develop considerably higher direct stiffness than straight seals.

Kleynhans [10] compared experimental and theoretical predictions for short honeycomb and smooth annular pressure seals. His work investigated how rotordynamic coefficients are influenced by six independent test parameters, pressure ratio across the seal, seal inlet pressure, rotor speed, seal inlet fluid rotation, seal clearance, and seal geometry (honeycomb cell width). He concluded that the code available for rotordynamic coefficient prediction was inadequate for predicting coefficients of honeycomb surfaces. Kleynhans [11] later worked to improve the prediction of force/motion relationship of gas annular honeycomb seals. ISOTSEAL an isothermal-flow, two-control-volume, bulk-flow rotordynamic analysis was developed as a result of his efforts. Kleynhans [11] presents extensive work on the friction factor model used for the solution of rotordynamic coefficients of ISOTSEAL. Kleynhans [11] also investigates acoustic models and develops a general-transfer-function model and method for identifying frequency dependent rotordynamic coefficients. Kleynhans and Childs [12] specifically discuss the acoustic influence of cell depth on the rotordynamic characteristics of smooth-rotor/honeycomb stator annular gas seals. Of particular interest during the analysis of smooth seals, was the influence of near acoustic resonance effects on the rotordynamic coefficients.

Weatherwax [13] tested honeycomb and smooth seals. The smooth seal test had two back-pressures and the inlet pressure was 17 bar. The central conclusion from his work is that practical application of rotordynamic coefficients and leakage rates determined for a seal in the centered position, are valid out to eccentricities of 0.5. He

goes on to say that this is an important consideration when performing a rotordynamics analysis of a machine, realizing that the seals and rotor will never run truly centered.

Sprowl [14] tested and compared straight smooth annular gas seals to honeycomb gas seals. He could not test at low back-pressures (high mass flow through the seal) resulting in choked flow or high preswirl due to instabilities in his test apparatus. Additionally, tests show essentially no frequency dependency of the rotordynamic coefficients.

Description of the Test Rig

The original test rig used has been thoroughly described in Childs and Hale [15]. The test rig was originally designed to test high-speed hydrostatic bearings. Figure 3 shows a cross section of the rig in its most recent configuration. The test rig has undergone many iterations allowing for the testing of various bearings and seals. The test rig has been used successfully in numerous other gas seal tests. Dawson et al. [16] describes the modifications made to the test rig to transform the hydrostatic bearing rig into the annular gas seal test stand. The current facility allows for testing annular gas seals with a supply air pressure of 70 bar (1015 psi). Two rotors were used to provide 0.2mm (8mils) and 0.1mm (4mils) radial clearance. The seals are aligned and held about the rotor via a stator housing, figure 4. Six axial pitch stabilizers and two orthogonally orientated hydraulic shakers position the stator housing about the rotor. The pitch stabilizers ensure concentricity of the seals to the rotor at each end of the housing. Each hydraulic shaker is located axially in the center of the stator and at forty-five degrees

from vertical in the angular direction. The hydraulic shakers are used to control the radial position of the stator. The rotor is supported at each end by a hydrostatic bearing.

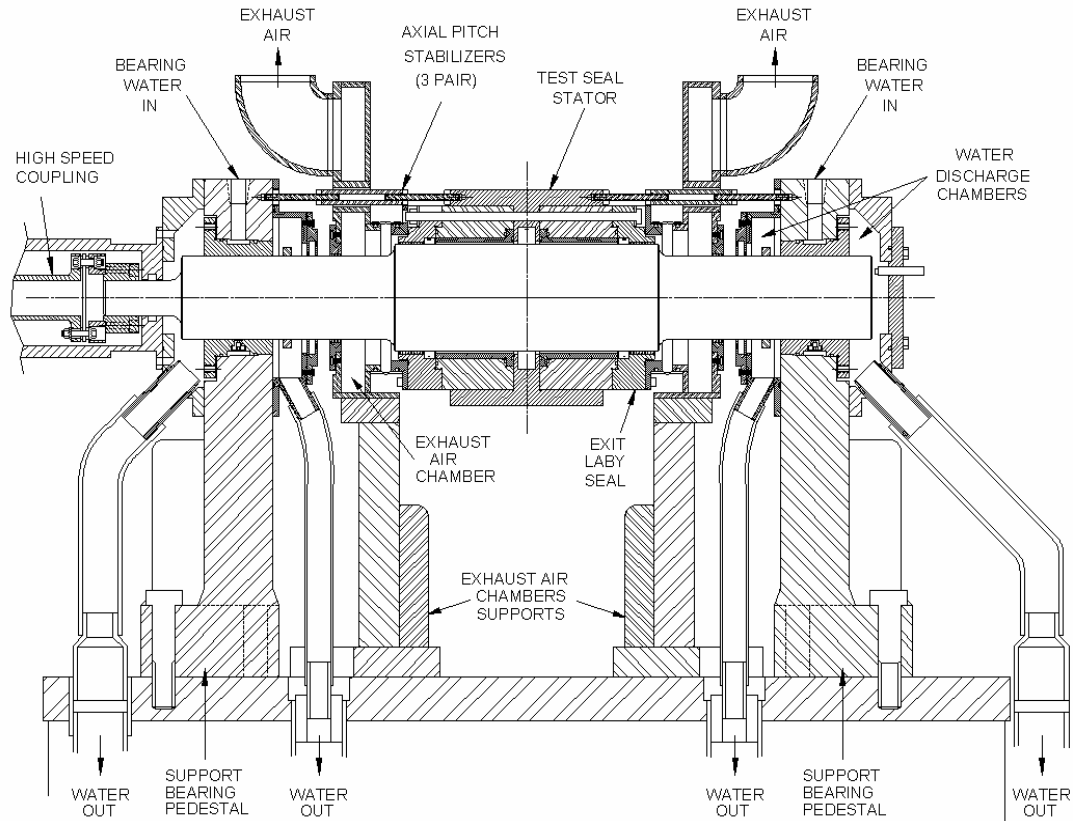


Fig. 3 Cross Sectional View of Test Apparatus

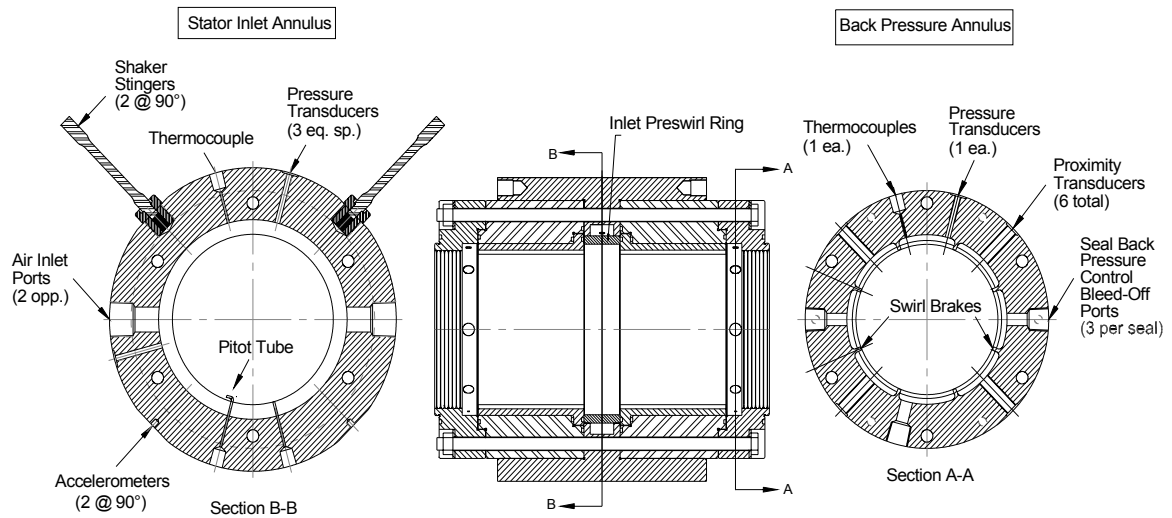


Fig. 4 Cross Section of Stator Housing

The high-pressure air is supplied to the center of the stator through a preswirl ring. The air then leaks to the exhaust ports through the seals being tested. The exhaust air pressure can be regulated enabling testing at different pressure ratios and leakage rates. The hydraulic shakers excite the stator with a pseudo-random waveform with frequencies that range from 20 Hz to a possible maximum 440 Hz in 10 Hz increments. During the excitation period, data are recorded from the following instruments:

- i.) proximity probes that give the relative displacement vectors between the stator and rotor
- ii.) force transducers that measure the force components required to shake the stator
- iii.) accelerometers that measure the acceleration of the stator.

These data are collected in two orthogonal directions parallel to the hydraulic shakers. The temperature and pressure of the working fluid are constantly monitored and recorded during the excitation period. In order to obtain data for medium and high preswirl cases for the test discussed within this thesis, four radial stiffeners were attached to the stator in the horizontal plane, forty-five degrees from the plane of the shaker stingers of figure 4. Asymmetric stiffness was introduced by the radial stiffeners with a total stiffness of 17.52 MN/m (100,000 lb/in). The added asymmetric stiffness increased the stability of the stator and allowed test to be completed that were previously not possible in testing by Sprowl [14].

Fluid Preswirl

The seals were tested at three fluid preswirl levels. The supply air is swirled around the shaft in the direction of shaft rotation utilizing a preswirl ring in the inlet annulus housing. Ports have been machined into the ring to achieve the desired preswirl ratio. Figure 5 shows a section of each preswirl ring. The zero preswirl ring utilizes radial ports, whereas the medium and high preswirl rings have smaller ports and larger relative injection angles.

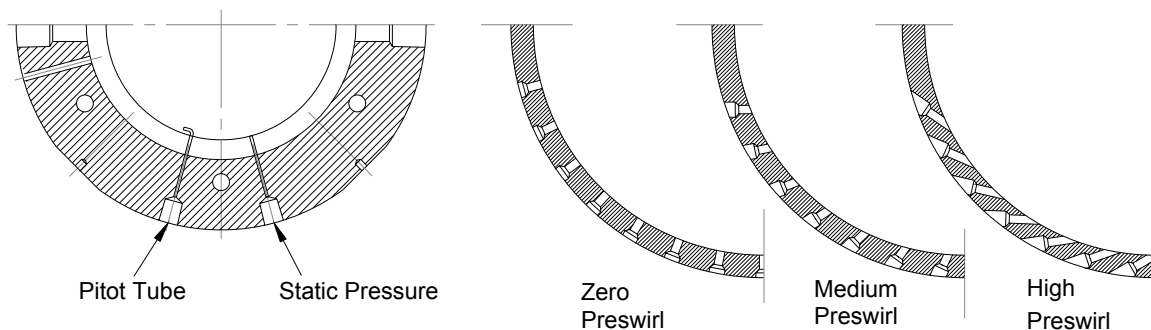


Fig. 5 Cross Section of Fluid Preswirl Rings

The preswirl ratio is the ratio of the circumferential fluid velocity to the rotor surface velocity. Sprowl [14] has shown that preswirl significantly affects the rotordynamic coefficients of smooth seals. As shown in figures 4 and 5, the inlet annulus is fitted with a Pitot tube and static pressure orifice. These tubes are connected to a differential pressure transmitter that displays the differential pressure head between the dynamic and static pressure. The differential pressure is converted to circumferential velocity using equation (2),

$$v_t = \sqrt{\frac{2g \cdot \rho_w \cdot H_w}{\rho_a}} \quad (2)$$

where H_w is the head in inches of water measured by the differential pressure transmitter, ρ_a is the density of air at the inlet conditions, and ρ_w is the density of water. The preswirl ratio is calculated using equation (3),

$$preswirl = \frac{v_t \cdot 60}{\pi \cdot D_r \cdot N} \quad (3)$$

where D_r is the diameter of the rotor and N is the rotor speed in revolutions per minute.

Seal Leakage

The primary function of the seals is to control leakage of the working fluid. The leakage is a function of the seal geometry, such as clearance, length, roughness, and machine operating conditions such as the pressure differential and rotor speed. A calibrated turbine flow meter located upstream of the test section is used to measure the leakage flow through the seals in Standard Cubic Feet per Minute (SCFM). The mass flow rates are calculated for the seals by converting the output of the turbine flow meter

and modifying the flow rates to compensate for temperature and pressure differences between test conditions and calibration conditions.

Calculation of Rotordynamic Coefficients

Rotordynamic coefficient identification is accomplished through dynamic testing. The stator housing is simultaneously shaken at multiple discrete frequencies using a psuedo-random waveform. The waveform is an ensemble of discrete sinusoids with frequencies every 10 Hz from 20 Hz to a potential maximum of 440 Hz. The phase of the sinusoids is optimized to provide a composite loading function with a high spectral-line energy to crest-factor ratio. Childs and Hale [15] provide a discussion of the power cross-spectral density method used to calculate a frequency-response function H_{ij} .

Dawson et al. [16], give equation (4) as the equation of motion for the stator mass M_s of figure 4 as

$$M_s \begin{Bmatrix} \ddot{x}_s \\ \ddot{y}_s \end{Bmatrix} = \begin{Bmatrix} f_x \\ f_y \end{Bmatrix} + \begin{Bmatrix} f_{xg} \\ f_{yg} \end{Bmatrix} \quad (4)$$

where \ddot{x}_s and \ddot{y}_s are the measured orthogonal stator accelerations, f_x and f_y are the measured shaker component input forces. Childs [17], states that the added mass terms for labyrinth gas seals are negligible, and the rotordynamic coefficients do not change for small perturbations of the rotor from the centered position. These two statements are significant to the validity of the model represented by equation (1). Additionally, the smooth annular seals are not expected to have frequency dependent rotordynamic coefficients. Equations (1) and (2) are combined and transformed into the frequency domain using a Fourier Transform resulting in impedances for the system as follows:

$$\begin{Bmatrix} F_x - M_s A_x \\ F_y - M_s A_y \end{Bmatrix} = \begin{bmatrix} H_{xx} & H_{xy} \\ H_{yx} & H_{yy} \end{bmatrix} \begin{Bmatrix} D_x \\ D_y \end{Bmatrix} \quad (5)$$

The elements of the frequency-response function \mathbf{H} are related to the coefficients in equation (1) by $\mathbf{H}_{ii} = K_{ii} + \mathbf{j} (\Omega C_{ii})$ for the direct stiffness and damping coefficients, and $\mathbf{H}_{ij} = k_{ij} + \mathbf{j} (\Omega c_{ij})$ for the cross-coupled damping and stiffness coefficients, where ω is the excitation frequency and $\mathbf{j} = \sqrt{-1}$. The above equations define the model in the frequency domain. To solve for the four unknowns in equation (5), two alternate shakes are performed in the orthogonal directions x and y yielding four complex equations and four unknowns given by equation (6).

$$\begin{bmatrix} F_{xx} - M_s A_{xx} & F_{xy} - M_s A_{xy} \\ F_{yx} - M_s A_{yx} & F_{yy} - M_s A_{yy} \end{bmatrix} = \begin{bmatrix} H_{xx} & H_{xy} \\ H_{yx} & H_{yy} \end{bmatrix} \begin{bmatrix} D_{xx} & D_{yx} \\ D_{xy} & D_{yy} \end{bmatrix} \quad (6)$$

Equations (5) and (6) are from Childs and Hale [15]. The subscripts ij of the force and displacement matrices correspond to response in the i direction due to dynamic loading in the j direction. The \mathbf{D}_{ij} coefficients are the relative displacements of the rotor and stator, \mathbf{A}_{ij} are the accelerations of the stator, and M_s is the mass of the stator. The data obtained during the seal test provide all of the above variables except the frequency-response function values \mathbf{H}_{ij} . The direct and cross-coupled frequency-response function \mathbf{H}_{ij} values are obtained from equation (6). Utilizing equation (7) the real part and the imaginary part of the impedance value is separated. The real part of the impedance gives the stiffness coefficients. The damping coefficients are found by fitting a straight line through the imaginary part of the impedance. The rotordynamic coefficients for the x and y directions are given by the following equations:

$$\begin{aligned}
 \operatorname{Re}(H_{xx}) &= K_{xx} & \operatorname{Re}(H_{yy}) &= K_{yy} \\
 \operatorname{Im}(H_{xx}) &= C_{xx} \cdot \Omega & \operatorname{Im}(H_{yy}) &= C_{yy} \cdot \Omega \\
 \operatorname{Re}(H_{xy}) &= k_{xy} & \operatorname{Re}(H_{yx}) &= k_{yx} \\
 \operatorname{Im}(H_{xy}) &= c_{xy} \cdot \Omega & \operatorname{Im}(H_{yx}) &= c_{yx} \cdot \Omega
 \end{aligned}
 \tag{7}$$

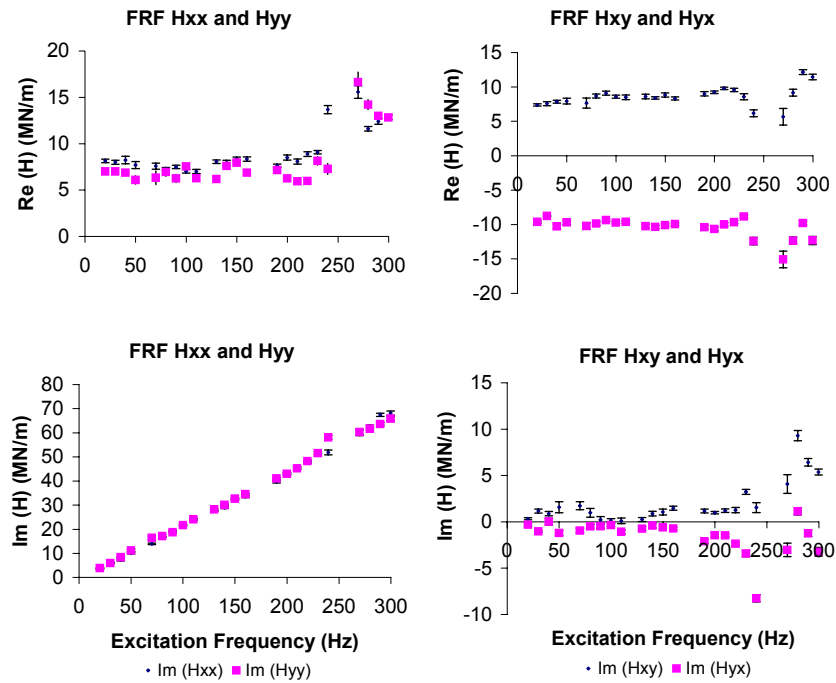


Fig. 6 Typical Elements of the Frequency-Response Function

Figure 6 shows a plot of typical frequency-response function elements obtained during a test. Frequency-response functions for both x and y directions are shown. Rotordynamic coefficients are determined from the frequency-response functions utilizing equation (7). Direct stiffness and direct damping frequency-response function elements are equal in

magnitude and sign for both direct stiffness and direct damping. Cross-coupled stiffness and cross-coupled damping are opposite in sign and nearly equal in magnitude.

Test Conditions

Experimental data were obtained for one set of smooth annular gas seals utilizing the Annular Gas Seal Test Stand previously described. The significant dimensions of the seals are shown in Table 1.

Table 1 Seal Dimensions

Seal Diameter	114.72 (mm)	4.516 (in.)
Seal Length	85.70 (mm)	3.374 (in.)

The seal diameter given in table 1 is an average of the seal diameter taken at three locations. The high clearance configuration utilized a 114.3 mm (4.500 inch) rotor to yield 0.21 mm (0.008 inch) radial clearance and the low clearance configuration utilized a 114.50 mm (4.508 inch) rotor to yield a 0.11 mm (0.004 inch) radial clearance. The shaft was manufactured with a ± 0.0051 mm (0.0002 inch) tolerance. A matrix of the actual tested conditions is shown in Table 2. The objective pressure ratios were 30%, 40%, 50%, and 65% for the 0.2mm clearance configuration and 17% and 50% for the 0.1mm configuration. Four pressure ratios at full inlet pressure, 70 bar (1015 psia) and three rotor speeds were obtainable only for the large clearance case with zero preswirl. For the large clearance case with medium preswirl, the inlet pressure was decreased to

18 bar (260 psia) due to instabilities. Likewise, the large clearance high preswirl configuration was also tested at the reduced inlet pressure of 18 bar (260 psia). Additionally the lowest back-pressure case could not be tested. For the small clearance case, only the zero preswirl configuration was tested at two pressure ratios. The seals were damaged during subsequent testing and no other data for the small clearance was obtainable.

Table 2 Test Conditions

Clearance	Preswirl	Rotor Speed	Pressure-Ratio
mm (inches)	-	RPM	P_e / P_{in}
0.1 (0.004)	Zero	10,200 15,200	0.17
0.1 (0.004)	Zero	10,200 15,200 20,200	0.53
0.2 (0.008)	Zero	10,200 15,200 20,200	.28 .39 .48 .65
0.2 (0.008)	Medium	10,200 15,200 20,200	.31 .41 .51 .65
0.2 (0.008)	High	10,200 15,200 20,200	.40 .50 .61

Additionally, baseline data were recorded with the test stand completely assembled without the seals. The same impedance identification method described above was used to identify the impedance values of the test rig without the seals. The impedances recorded in the baseline test were subtracted from the seal test impedance

values. This step isolates the results caused by the seals only, and the rotordynamic coefficients and leakage due only to the seals may be found. The baseline data are recorded with zero preswirl only. The objective of subtracting the baseline data is to remove the external damping and stiffness attributed to the air inlet and exhaust hoses, pitch stabilizers, radial stiffeners, and stingers. Additionally the leakage effects of the exit labyrinth seals were subtracted. The stator inlet pressure was varied and baseline data were recorded at 3.45 bar (50 psi) increments. During baseline subtraction, the inlet pressure to the exit labyrinth seal was matched with the corresponding exit pressure from the test seal. The exit labyrinth seals are short, approximately 25.4 mm (1 inch) in length and have a swirl brake installed immediately upstream. Sample baseline measurements are shown in appendix A. The rotordynamic coefficients, leakage, and choked flow conditions found will be compared with theoretical calculations of a code developed at the Turbomachinery Laboratory by Kleynhans [11] in subsequent sections.

Test Data Uncertainty

The primary concern for uncertainty is that induced by the instrumentation. Efforts have been made to minimize uncertainty through calibration before installation. Daily calibrations are performed on the pressure transducers and accelerometers once they are installed before data acquisition begins. Uncertainty error for static parameters have been estimated by Kurtin et al. [18] and are presented in table 3.

Table 3 Uncertainty of Measured Parameters

Parameter	Uncertainty
Shaft Speed	± 10 rpm
Pressure	± 3.747 kPa
Flow Rate	± 0.177 liters / min
Eccentricity Ratio	± 0.03

The uncertainty of the experimentally determined impedance values varies strongly with excitation frequency. For the dynamic measurements, an uncertainty test was performed for each seal by running ten identical tests to obtain an average and ± 1 standard deviation at each frequency of interest, Dawson et al. [16]. Data points taken at 50, 60, 120, 170, 180, 240, 250, 260, 270 Hz are typically removed from the impedance data due to high uncertainty induced by electrical noise and close proximity to running speed. Uncertainty is calculated for both the experimental impedances and the baseline impedances. The resulting uncertainty is calculated as follows:

$$Uncertainty_{total} = \sqrt{Uncertainty_{baseline}^2 + Uncertainty_{test}^2} \quad (8)$$

The error bars shown at each frequency in the results represent ± 1 standard deviation for each frequency. Detailed specifications of the instruments used in the testing are in appendix B.

EXPERIMENTAL RESULTS

The results presented are the average of the coefficient data obtained from the x and y directions after baseline subtraction. Examples of the baseline data are in appendix A. Each set of data graphed represents a common pressure ratio and rotor speed at three levels of preswirl, unless otherwise noted. Only the zero preswirl configuration was stable enough to allow testing at the full inlet pressure for the 0.2mm (8 mil) clearance. At the medium and high preswirl configurations, the inlet pressure was decreased to 18 bar (260 psia). The stiffness coefficients have been non-dimensionalized and the damping coefficients have been normalized in accordance with equation (9). Units for the variables used in equation 9 are given in table 4.

$$K^* = K \left(\frac{C_r}{\Delta P \cdot D_s \cdot L} \right) \tag{9}$$

$$C^* = C \left(\frac{C_r}{\Delta P \cdot D_s \cdot L} \right)$$

Table 4 Variables Used for Non-dimensional and Normalized Stiffness and Damping

Variable		Units
Stiffness	K	MN/m
Damping	C	N-s/m
Radial Clearance	C_r	m
Pressure	P	N/m^2
Seal Diameter	D_s	m
Seal Length	L	m

The non-dimensional and normalized coefficients allow for comparison of the results from the various tests at different inlet pressures. Upon analyzing the graphs in the following sections, one is to be cautious with the interpretation of the results. Although the coefficients have been non-dimensionalized and normalized, the data from all three preswirl cases are not directly comparable since the forces within the seals are only roughly proportional to the ΔP across the seal and the fluid density within the seal. Data for test completed at 0.1mm clearance is limited to only two back-pressure ratios at the zero preswirl configuration. The rotor rubbed the seals during testing at the 0.1mm clearance. The seals were damaged such that no further testing could be accomplished. The 0.1mm clearance data will be presented, however, comparison of data between the test conditions will be limited. The following sections will discuss and compare the experimental results for non-dimensional direct stiffness K^* , non-dimensional cross-coupled stiffness k^* , normalized direct damping C^* , and normalized effective damping C^*_{eff} . Coefficients for cross-coupled damping are not discussed. The experimental values of cross-coupled damping are widely scattered, and no clear trend is apparent. The force produced by the influence of cross-coupled damping is much smaller than the other rotordynamic coefficients, thus its influence on rotordynamic calculations is rather insignificant Nelson et al. [9]. This statement was found to be accurate for the experimental data presented in the following sections.

Direct Stiffness

The direct stiffness values are estimated from the real impedance values as given by equation (7) and non-dimensionalized by the method of equation (9). The resulting

non-dimensional stiffness values versus excitation frequency are plotted in figure 7. There are 12 graphs represented in figure 7. The columns of graphs are arranged in increasing rotor speed from left to right. The rows of graphs are arranged in increasing back-pressure from top to bottom. The lowest back-pressure corresponds to the largest pressure drop. The data plotted are the experimental stiffness values obtained at the respective rotor speed, back-pressure, excitation frequency, and preswirl configuration. The 30% back-pressure case only contains data for the zero and medium preswirl cases. The 30% back-pressure high preswirl configuration was not tested. The direct stiffness force is a radial force that acts to center the rotor and can influence the rotor's critical speed, Kleynhans [10]. The direct stiffness of a gas seal does not directly contribute to the rotordynamic stability of the system. Upon analyzing figure 7, one can see there is virtually no change in direct stiffness values with an increase in rotor speed. Direct stiffness increases with increasing back-pressure in all configurations. Although the back-pressure was held the same for all preswirl configurations, the pressure drop across the seals at medium and high preswirl was significantly less. Direct stiffness increases slightly with increasing excitation frequency. This increase is discussed in the experimental and predictions section to follow. At the highest pressure ratio, the direct stiffness begins to decrease after approximately 200 Hz suggesting there may be a slight frequency dependent nature in this region of operation.

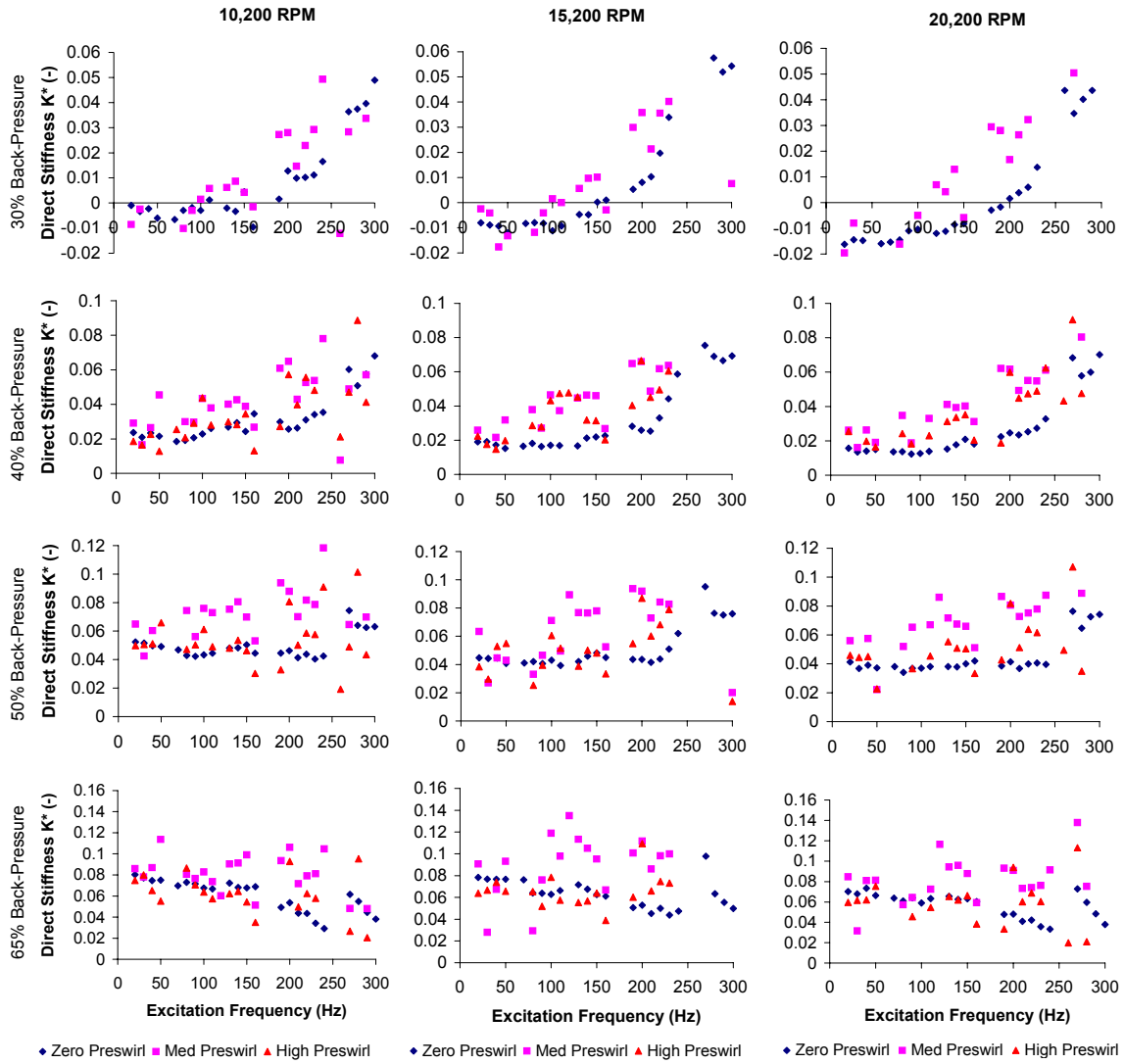


Fig. 7 Non-Dimensional Direct Stiffness vs. Excitation Frequency, $C_r = 0.2\text{mm}$

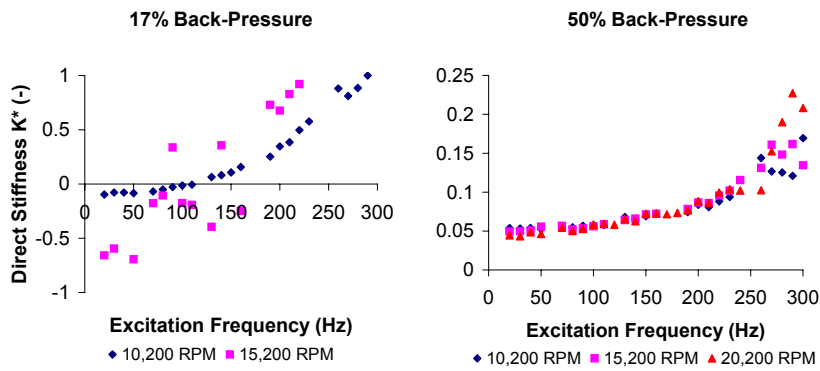


Fig. 8 Non-Dimensional Direct Stiffness vs. Excitation Frequency, Zero Preswirl, $C_r = 0.1\text{mm}$

Figure 8 shows the only direct stiffness values obtained for the 0.1mm clearance case. Both back-pressures are at zero preswirl and an inlet pressure of 70 bar. There is little change in K with increasing speed at the 17% back-pressure and no significant change of direct stiffness values at 50% pressure ratio with increasing speed. At the 0.1mm clearance, the direct stiffness values appear to be somewhat frequency dependent. Comparing the 50% zero preswirl cases of figures 7 and 8, the 0.1mm K values are lower but tend to increase with increasing frequency beyond 150 Hz.

Cross-Coupled Stiffness

Rotordynamic stability is directly influenced by cross-coupled stiffness. As figure 2 shows, cross-coupled stiffness acts as a component of the tangential follower force that is a driver of instability. In the experimental data observed, all cross-coupled stiffness terms act as destabilizing forces. As figure 9 shows, cross-coupled stiffness only marginally increases with increasing rotor speed. Figure 9 shows large increases of cross-coupled stiffness with increasing preswirl as expected. The zero preswirl and the medium and high preswirl case cannot be directly compared. The medium and high preswirl cases are at reduced inlet pressure and have radial stiffeners added to the stator. Experimental values for cross-coupled stiffness increase with increasing preswirl, a result consistent with Sprowl [14] and Weatherwax [13].

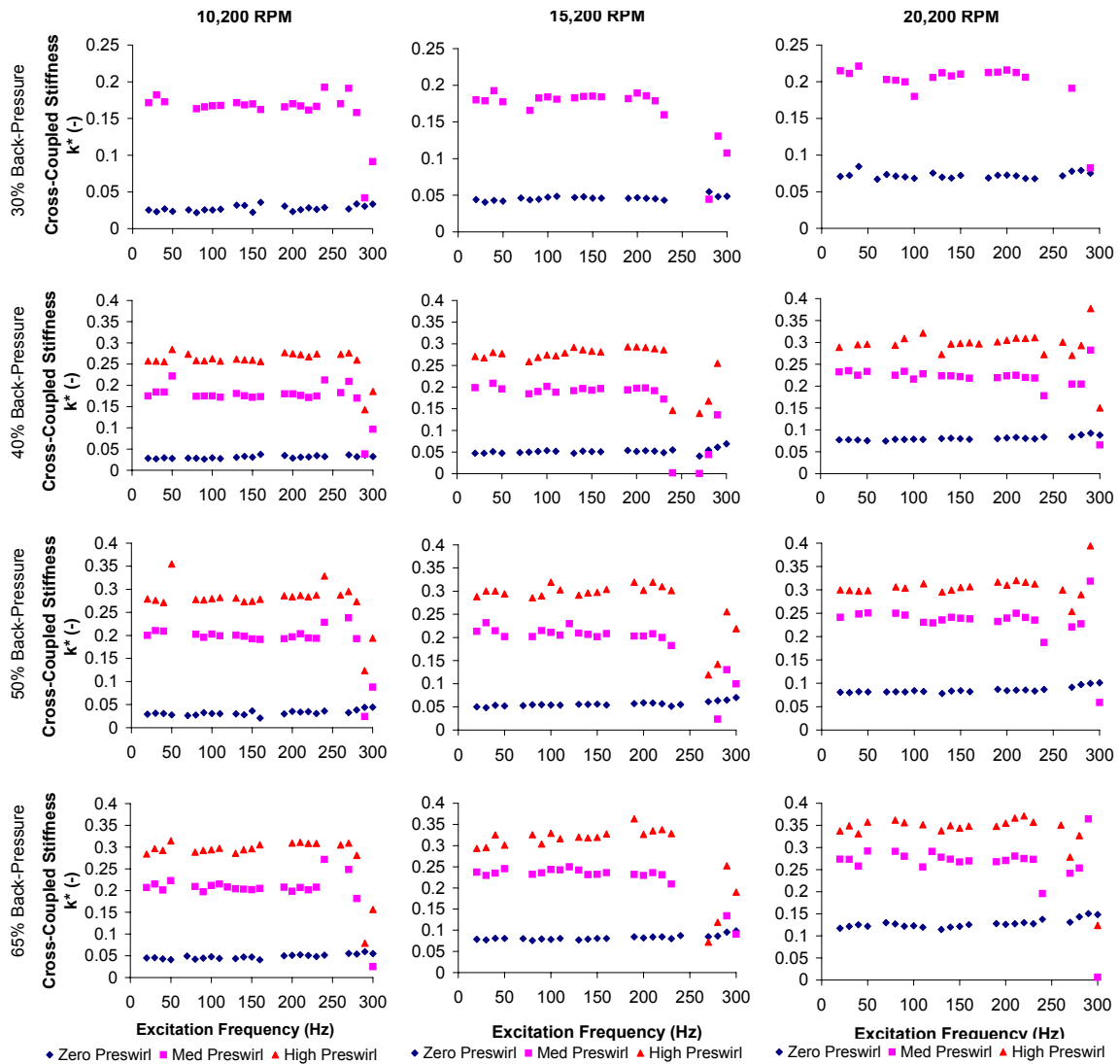


Fig. 9 Non-Dimensional Cross-Coupled Stiffness vs. Excitation Frequency, $C_r = 0.2\text{mm}$

Sprowl [14] suggests cross-coupled stiffness is more sensitive to rotor speed under zero preswirl conditions than at medium and high preswirl conditions, and a large jump in magnitude from the zero preswirl case to the medium preswirl case in his results is due to this sensitivity. The data shows a frequency independent nature except at the highest back-pressure ratio. As with the direct stiffness values, the cross-coupled values

begin to slightly decrease as excitation frequency increases beyond 200 Hz, suggesting a slight frequency dependent nature. The cross-coupled stiffness values increase only slightly with increasing back-pressure at any given rotor speed except there is a relatively large increase in cross-coupled stiffness for the zero preswirl case upon transitioning to the 65% back-pressure configuration.

Figure 10 shows cross-coupled stiffness values for the 0.1mm clearance case at two back-pressures and only the zero preswirl case. The k^* values for the 17% back-pressure 15,200 rpm case, although obtained, were random. The instability and subsequent rub event occurred at this operating condition. There was no pattern to the data points and they were subsequently deleted. The frequency independent nature continues to be prevalent at the lower clearance. Given only the 10,200 rpm case, there is a small increase in cross-coupled stiffness with increasing back-pressure. The k^* values at 0.1mm clearance are all larger than the corresponding k^* values at the 50% back-pressure zero preswirl condition of the 0.2mm clearance.

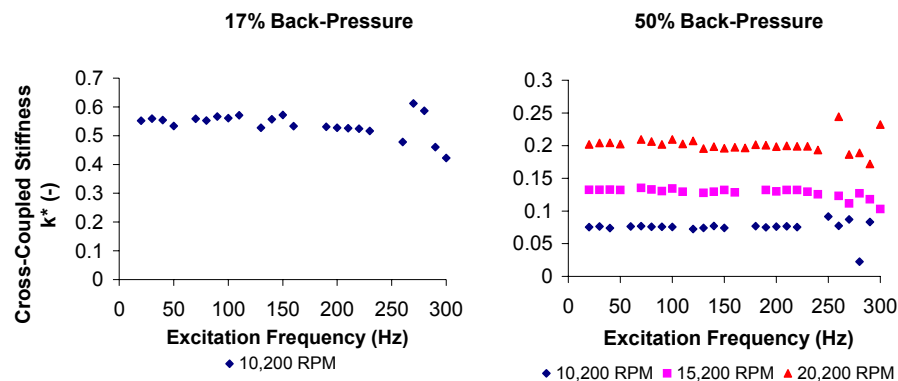


Fig. 10 Non-Dimensional Cross-Coupled Stiffness vs. Excitation Frequency, Zero Preswirl, $C_r = 0.1\text{mm}$

Direct Damping

Direct damping directly influences the stability of the rotordynamic system. A positive direct damping, as shown on figure 2, opposes the follower force and has a stabilizing effect on the system. Figure 11 shows direct damping values only change slightly with a change in preswirl. No significant changes in direct damping are noticed with changes in rotor speed or back-pressure. Frequency independence is maintained throughout the various cases. The only notable occurrence is at the 50% and 65% back-pressure ratios. The direct damping values tend to be lower at excitation frequencies less than 60 Hz and then maintain a stable value or show a slight increase throughout the remaining frequency range. The direct damping values for the 0.1mm case are shown in figure 12. The 15,200 rpm values have been eliminated from the 17% back-pressure case, as with the cross-coupled stiffness terms, the data was widely scattered with no discerning trend. Compared with the 0.2mm case, the reduced clearance case shows an increase in direct damping at the 50% back-pressure zero preswirl configuration. At the 10,200 rpm instance, direct damping of the 0.1mm clearance case is nearly twice as large as the direct damping at the 0.2mm clearance case. Direct damping tends to become more scattered with increasing rotor speed at high excitation frequencies, particularly for the medium and high preswirl configurations.

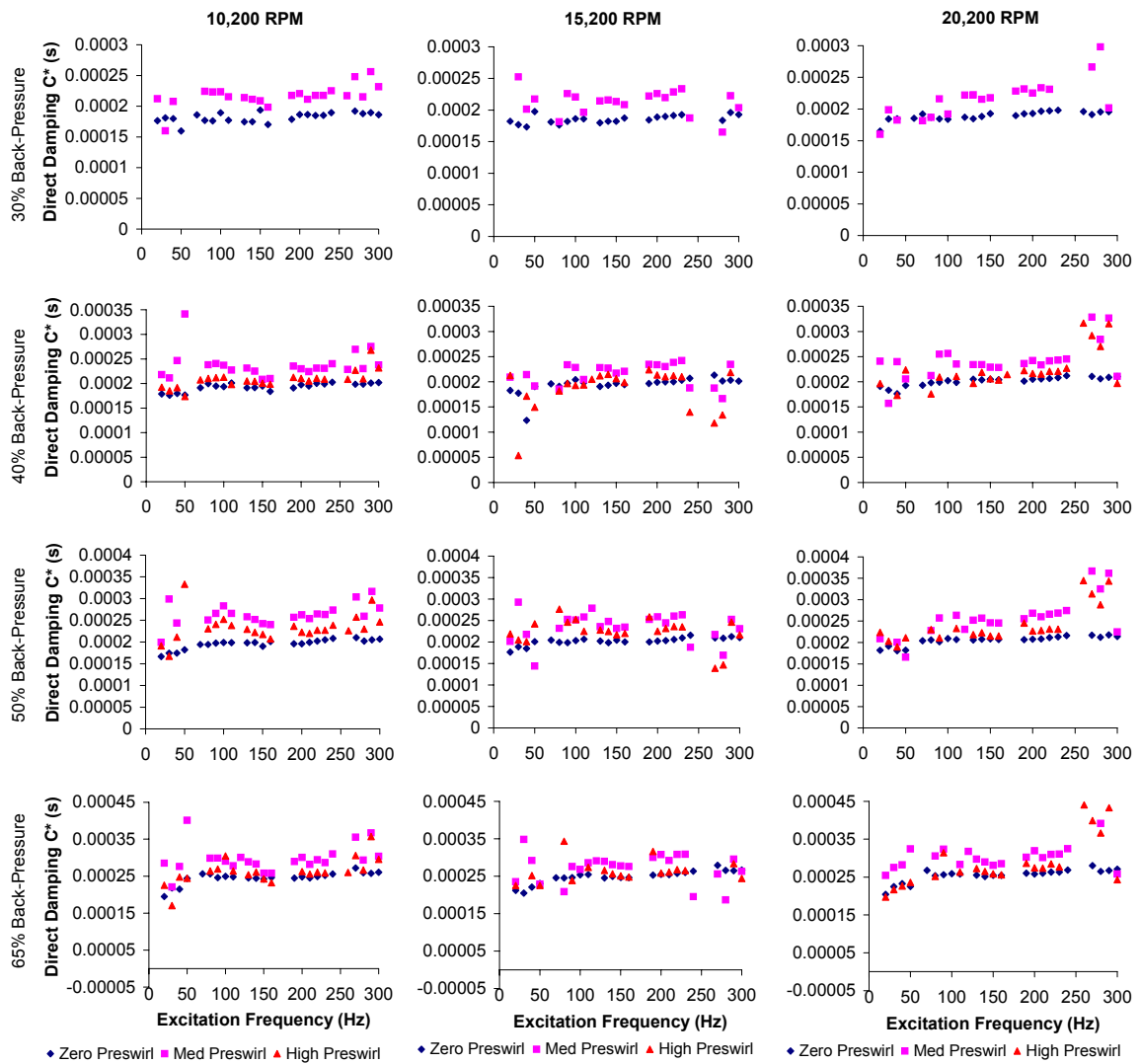


Fig. 11 Normalized Direct Damping vs. Excitation Frequency, $C_r = 0.2\text{mm}$

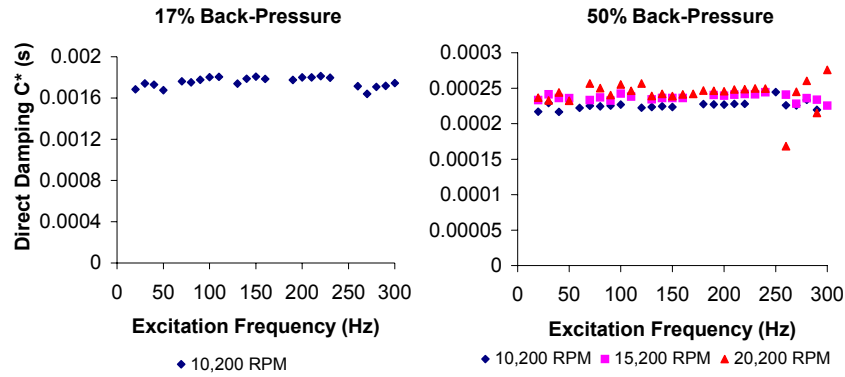


Fig. 12 Normalized Direct Damping vs. Excitation Frequency, Zero Preswirl, $C_r = 0.1\text{mm}$

Effective Stiffness

Effective stiffness is given in equation (10) as:

$$K_{eff} = K(\Omega) + c(\Omega)\Omega - M(\Omega)\Omega^2 \quad (10)$$

and non-dimensionalized using equation (9) to obtain K_{eff}^* . The added cross-coupled damping term is very small compared to the direct stiffness term. The effective stiffness is the effective centering force for the system. Effective stiffness values are nearly identical to the direct stiffness values of figure 7 and change with excitation frequency, preswirl, and back- pressure in the same manner as direct stiffness. No discernable differences can be realized by analyzing additional graphs. Therefore, effective stiffness plots are not included.

Effective Damping

The effective damping can be used as a stability indicator for the system.

Effective damping is defined by equation (11) as follows:

$$C_{eff} = C(\Omega) - \frac{k(\Omega)}{\Omega} \quad (11)$$

and normalized by applying equation (9) to obtain C_{eff}^* . A negative value of effective damping indicates that the cross-coupled stiffness term is dominant. As shown in figure 2, cross-coupled stiffness is a follower force, or a driver of instability. Figure 13 shows the effective damping at the 0.2mm operating conditions. Effective damping is highly influenced by preswirl. As the preswirl is increased, the effective damping values decrease, and the crossover from negative to positive values of effective damping occurs at a higher excitation frequency. These results agree with previous results by Sprowl [14]. There is a slight decrease of C_{eff}^* with increasing rotor speed accompanied by a movement in the crossover point to higher excitation frequencies. Back-pressure changes have very little influence on effective damping.

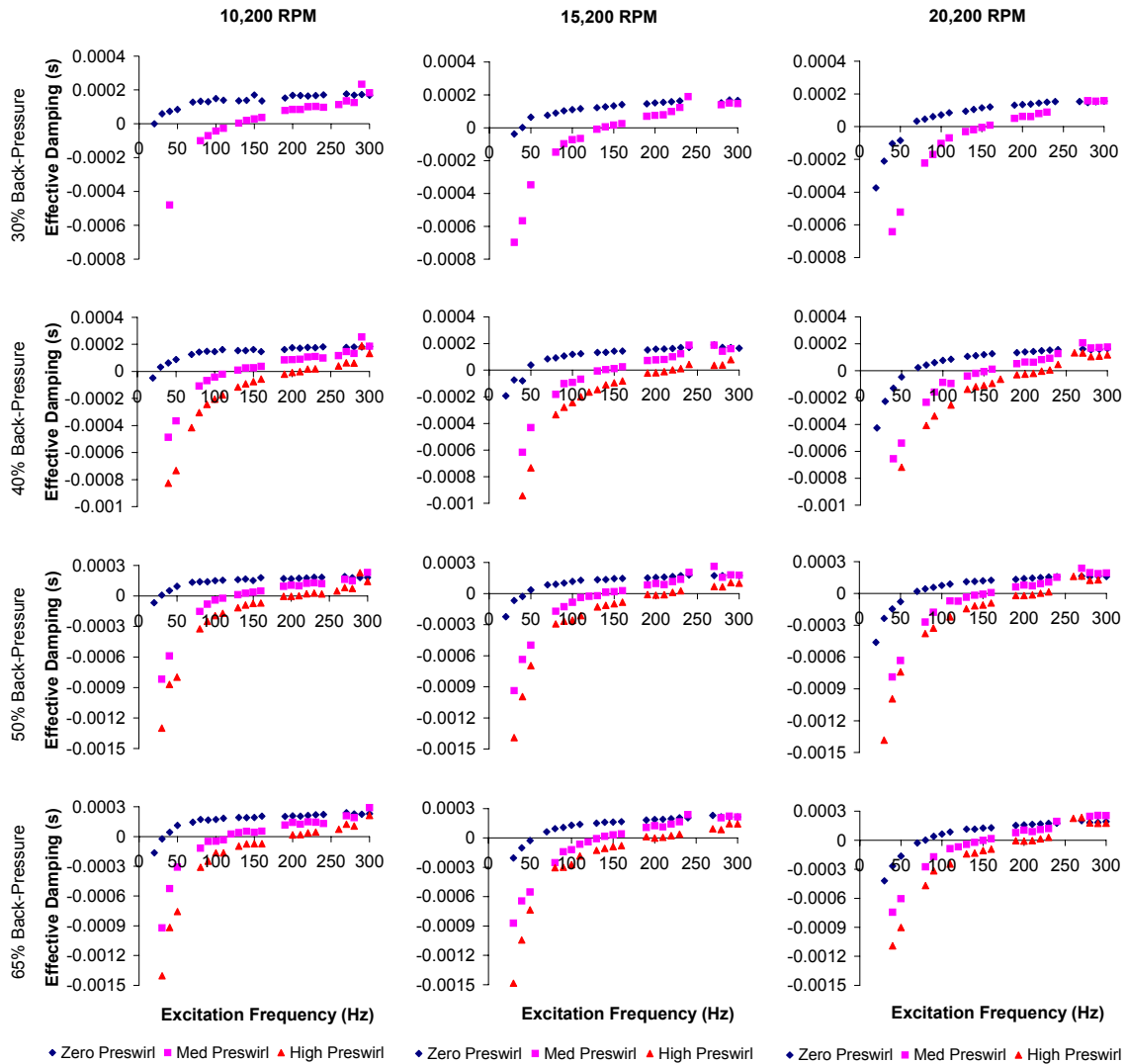


Fig. 13 Normalized Effective Damping vs. Excitation Frequency, $C_r = 0.2\text{mm}$

Figure 14 shows how the effective damping changes with a reduction in the clearance for the 17% and 50% back-pressure zero preswirl configurations. The effective damping values crossover at a lower excitation frequency in the 0.1mm clearance case and obtain higher positive values at higher excitation frequencies than the 0.2mm case. The effective damping values begin to converge to a uniform value at high excitation frequencies for all rotational speeds in the 0.1mm case.

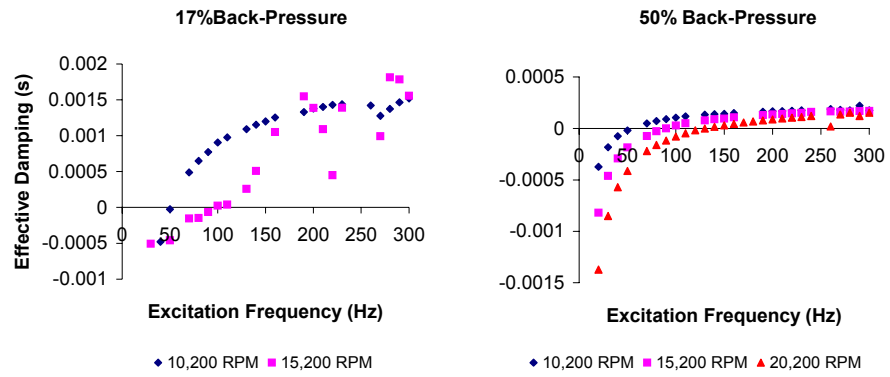


Fig. 14 Normalized Effective Damping vs. Excitation Frequency, Zero Preswirl, $C_r = 0.1\text{mm}$

EXPERIMENT VERSUS PREDICTIONS

In the following sections, experimental results will be compared with theoretical predictions from ISOTSEAL, a program developed at Texas A&M University Turbomachinery Laboratory. ISOTSEAL (constant temperature, two control volume, annular gas seal code) uses a two-control volume model to predict frequency dependent rotordynamic coefficients and leakage. ISOTSEAL integrates equation (11) over discrete frequencies to find the radial and tangential impedances.

$$\begin{aligned}
 I_r(\Omega) &= -\pi \int_0^1 \text{Re}[P(\Omega)] dz \\
 I_\theta(\Omega) &= -\pi \int_0^1 \text{Im}[P(\Omega)] dz
 \end{aligned}
 \tag{12}$$

A regression analysis of the resulting impedance values is completed. If the impedance values correlate well, the frequency independent model of equation (1) is used to predict rotordynamic coefficients. However, if the values do not correlate, the mathematical model and subsequent rotordynamic coefficient identification follow that presented in Kleynhans [11], whereby a transfer function is utilized in the two-control volume model of ISOTSEAL and frequency dependent rotordynamic coefficients are defined. Smooth seals are not expected to be frequency dependent, however, some experimental data does appear to be frequency dependent, and theory predicts frequency dependent characteristics for some configurations in the following sections. ISOTSEAL input data includes the operating conditions, seal geometry, entrance losses and exit recovery factors, and empirical rotor and stator friction coefficients used in the program's Blasius shear stress model Dawson and Childs [19]. The friction factor

model utilized in the development of the theoretical predictions is given by equation (13).

$$f = n Re^m \quad (13)$$

The constants used during testing were, $n = 0.0586$ and $m = -0.217$ for both the rotor and seal surfaces. These constants are from extensive flat plate test results by Ha and Childs [20]. Each test condition will be presented with its respective theoretical predicted values. The experimental values are shown with ± 1 sigma error bars. The rotordynamic coefficients presented in the following sections have not been non-dimensionalized or normalized unless otherwise noted.

Direct Stiffness

Figure 15 shows the experimental and theoretical direct stiffness values for each test configuration. All test of figure 15 were completed at zero preswirl. The theory under-predicts direct stiffness for all back-pressure cases except the highest back-pressure case at zero preswirl. The considerable under-prediction and slight increase of K with increasing frequency for the low back-pressures, agrees with Sprowl [14]. The increase in the experimental and predicted values is due to the direct inertia. Kleynhans [11], states that previous analyses assumed that because the fluid was gas, the density of the fluid was low and thus, the inertia effect M was low. Kleynhans [11], goes on to state that the mass-like term is not fluid inertia but rather a stiffening effect due to fluid compressibility, and develops an explanation via an acoustical study. At the higher excitation frequencies, the effective sonic speed is reduced and acoustic resonances appear. The increase of direct stiffness with excitation frequency in the frequency

independent cases is an indication that experimental conditions are approaching resonance. The direct inertial term M is incorporated as a negative mass for frequency independent conditions and as a positive mass for frequency dependent conditions. Acoustic influence of seal geometry is discussed in Kleynhans and Childs [12]. Equation (14) is used to plot the theory trend line.

$$K_{theory} = K(\Omega) - M(\Omega)\Omega^2 \quad (14)$$

All cases are predicted utilizing the frequency independent single control volume, bulk flow model in ISOTSEAL except the 15,200 rpm and 20,200 rpm cases at the 65% back-pressure. Smooth seals are not supposed to be frequency dependent, however, the program correctly predicts a slight frequency dependent nature of K at the two test cases mentioned. Theory predicts choked flow for the 30% back-pressure tests with zero preswirl. Sprowl [14] suggest that this choked flow condition may be the cause of the negative stiffness values.

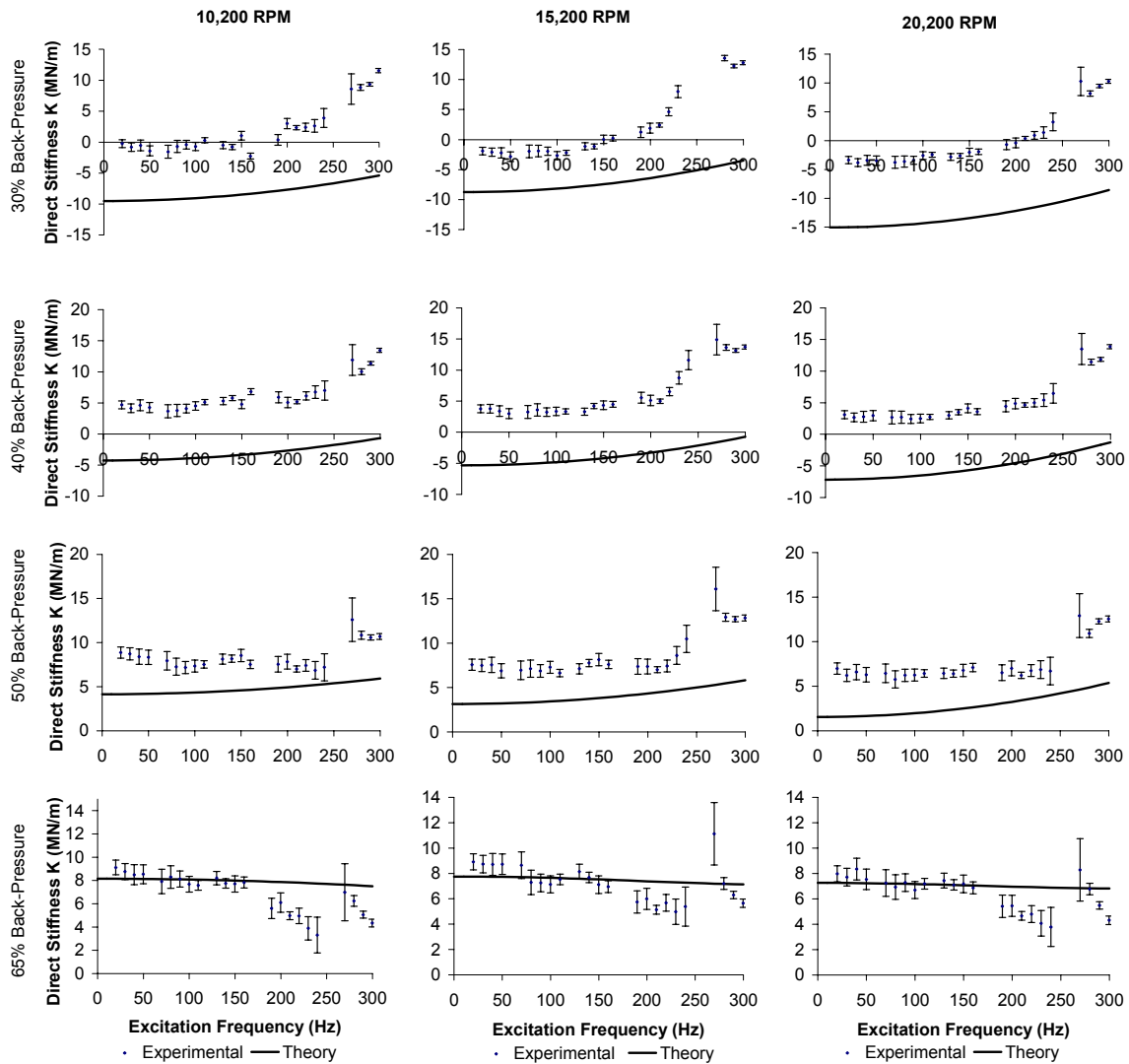


Fig. 15 Experimental and Theoretical Direct Stiffness vs. Excitation Frequency, Zero Preswirl, $C_r = 0.2\text{mm}$

Theory under-predicts direct stiffness at all operating conditions of figure 16, however, the under-prediction is much less than in figure 15. Preswirl has been increased to the medium preswirl configuration, inlet pressure decreased, and radial stiffeners employed. Theory predicts the direct stiffness well at 40%, 50%, and 65% back-pressures. Additionally, the theory predicts the 15,200 rpm and 10,200 rpm 65%

back-pressure cases to be frequency dependent. However, the dependent nature predicted is very weak. All 30% back-pressure cases are predicted to have choked flow. Yet, negative values of stiffness are not seen at the 30% back-pressure medium preswirl configuration as they are with choked flow at the 30% back-pressure zero preswirl configuration.

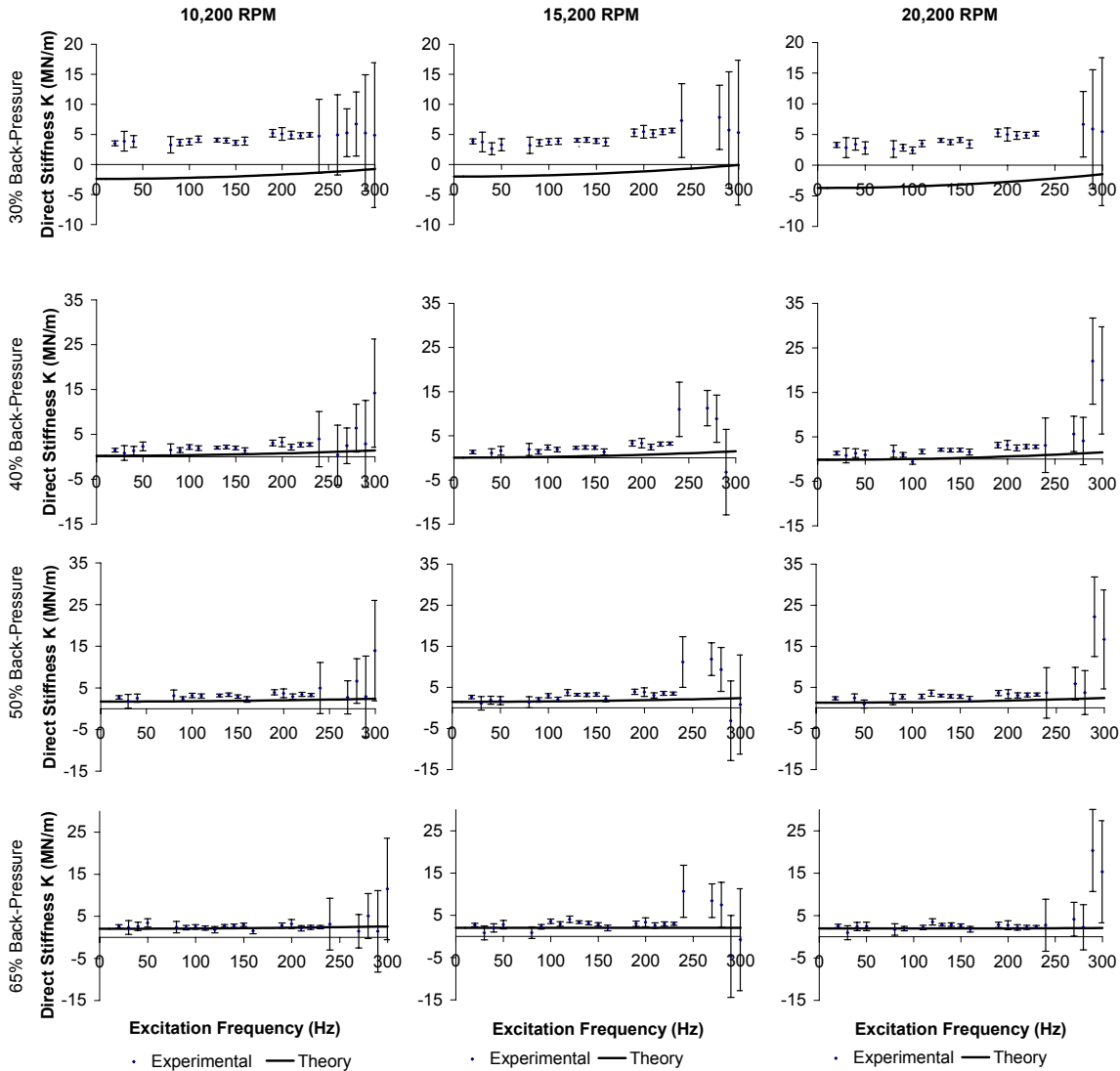


Fig. 16 Experimental and Theoretical Direct Stiffness vs. Excitation Frequency, Medium Preswirl, $C_r = 0.2\text{mm}$

Direct stiffness is predicted very well in all cases of figure 17. There are no predicted frequency dependent direct stiffness values at the high preswirl case. Theory predicts no configurations to have choked flow. Theory under-predicts direct stiffness at the reduced clearance of 0.1mm. Figure 18 shows the experimental direct stiffness has some frequency dependent characteristics that the theory does not detect. Theory predicts choked flow for the 17% back-pressure configuration. Theoretical predictions are slightly better at 50% back-pressure than 17% back-pressure.

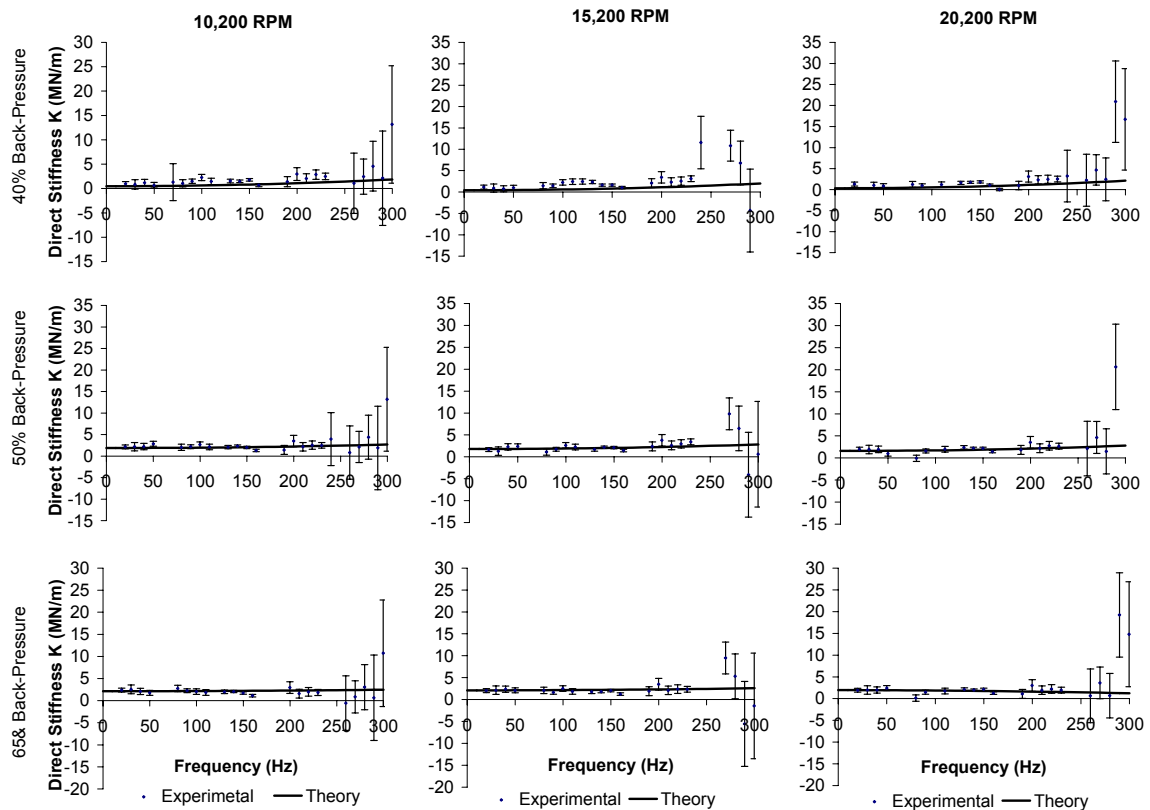


Fig. 17 Experimental and Theoretical Direct Stiffness vs. Excitation Frequency, High Preswirl, $C_r = 0.2\text{mm}$

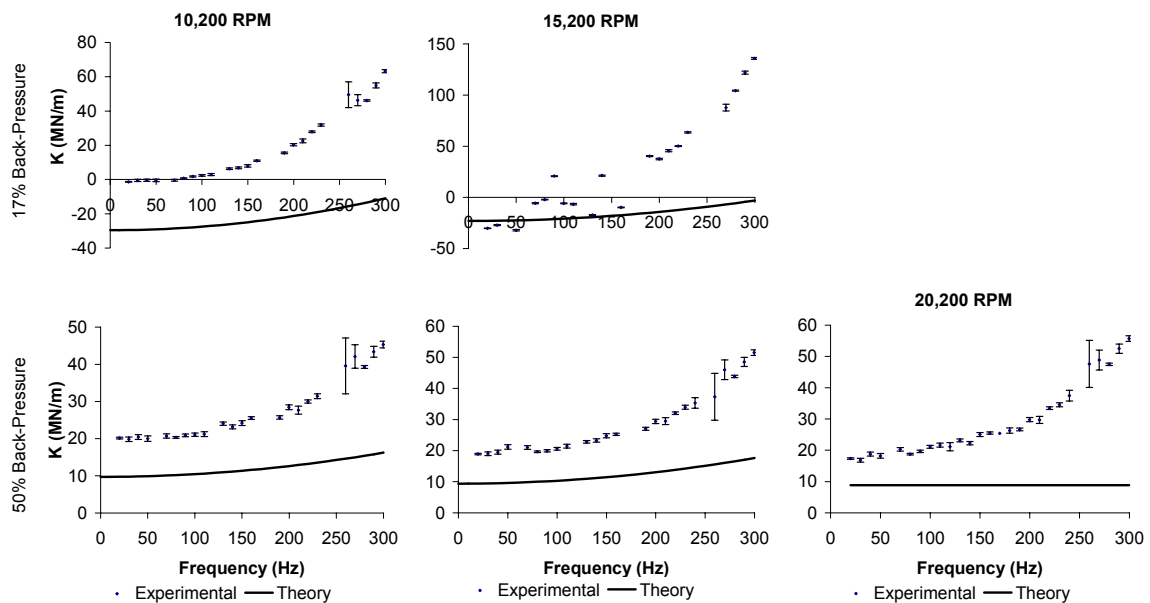


Fig. 18 Experimental and Theoretical Direct Stiffness vs. Excitation Frequency, Zero Preswirl, $C_r = 0.1\text{mm}$

Cross-Coupled Stiffness

Cross-coupled stiffness is under-predicted by theory at all operating conditions of figure 19. Theory predicts an increase in k^* with increasing rotor speed. The 15,200 rpm and 20,200 rpm 65% back-pressure cases are predicted to be frequency dependent. The frequency dependent nature is very weak, however, the general trend in predicted values for the frequency dependent cases is correct. The variance of the baseline cross-coupled stiffness values combine with the variance of the test seal cross-coupled stiffness to result in large the large variance in the following cross-coupled stiffness figures. The cross-coupled stiffness terms of baseline data are typically small, however, addition of the radial stiffeners greatly increases the cross-coupled stiffness components of the baseline data thereby greatly increasing the variance in the baseline data.

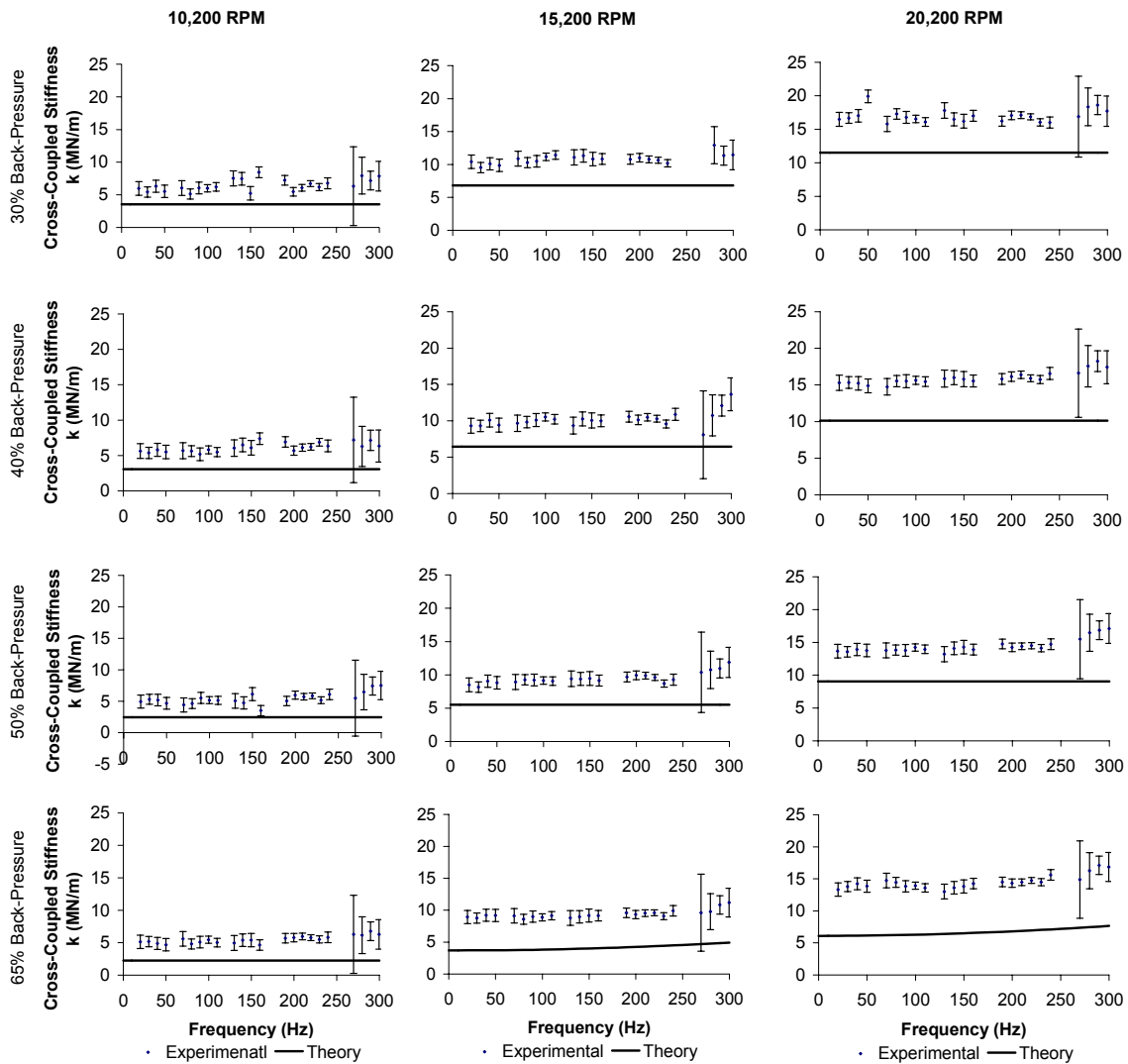


Fig. 19 Experimental and Theoretical Cross-Coupled Stiffness vs. Excitation Frequency, Zero Preswirl, $C_r = 0.2\text{mm}$

Theoretical predictions of cross-coupled stiffness are slightly better for the medium preswirl configuration, figure 20, and the high preswirl configuration, figure 21, than the zero preswirl configuration. Theory under-predicts all cross-coupled stiffness values at all operating conditions. Theory predicts a weak frequency dependent nature for the 15,200 rpm and 20,200 rpm 65% back-pressure cases in figure 19. No frequency

dependent characteristics are predicted for the high preswirl case. Appendix A shows how the added radial stiffness is resolved into direct and cross-coupled components.

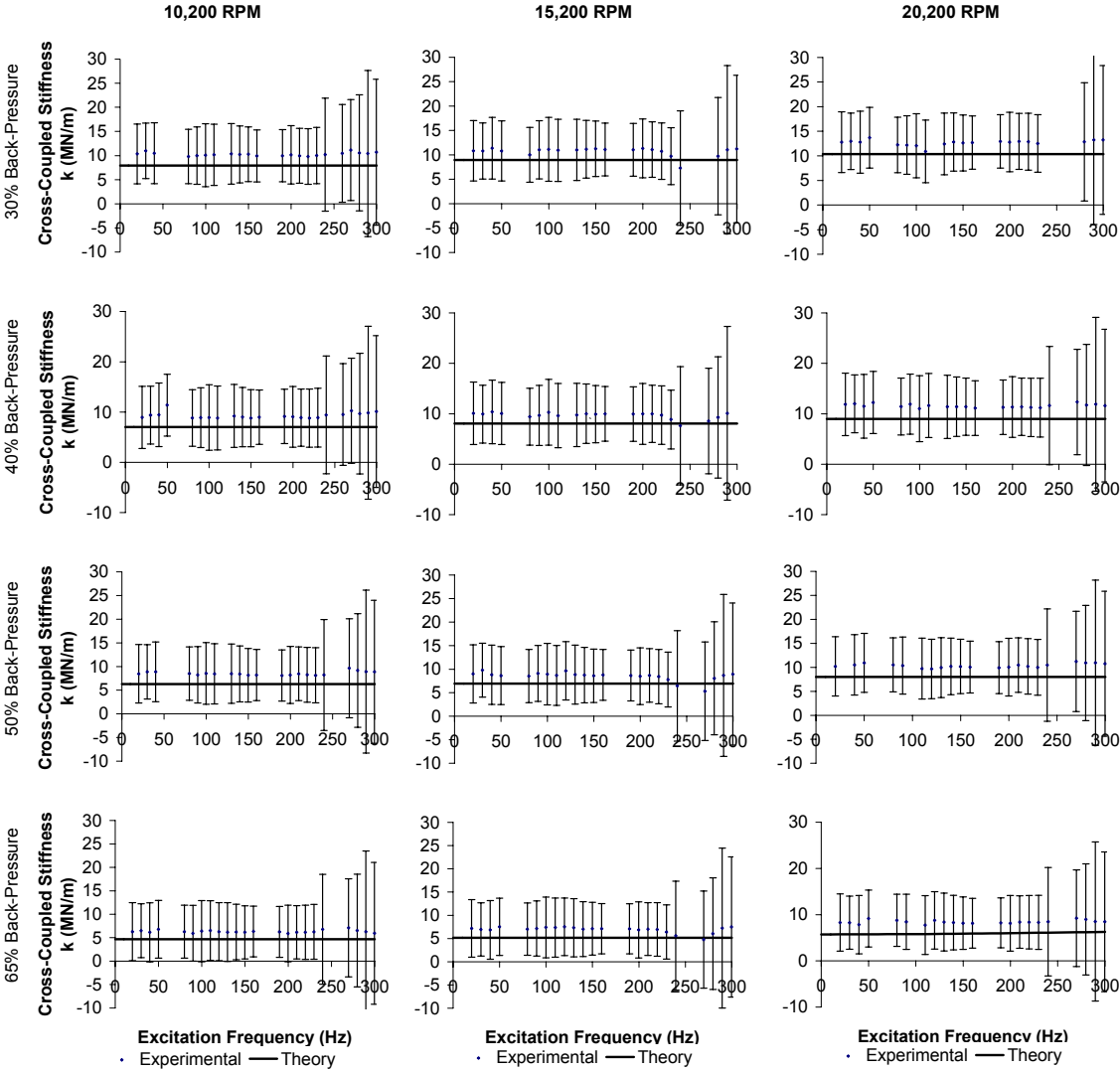


Fig. 20 Experimental and Theoretical Cross-Coupled Stiffness vs. Excitation Frequency, Medium Preswirl, $C_r = 0.2\text{mm}$

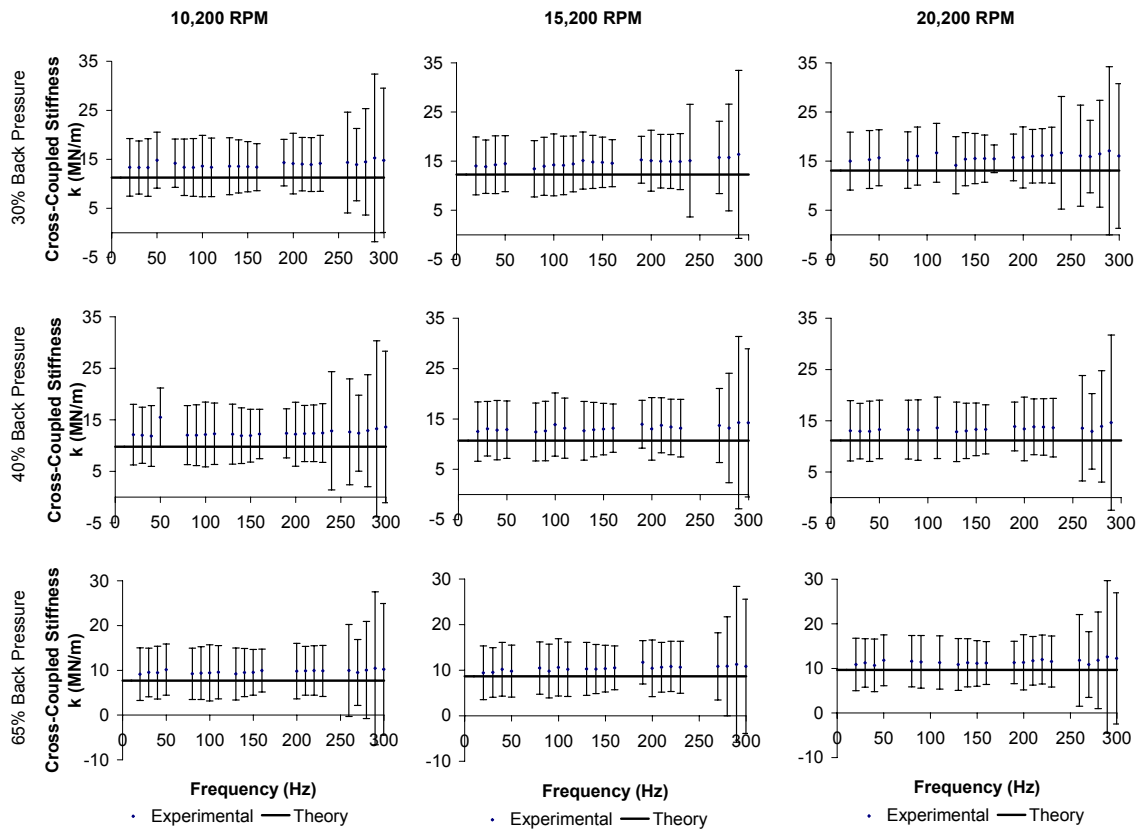


Fig. 21 Experimental and Theoretical Cross-Coupled Stiffness vs. Excitation Frequency, High Preswirl, $C_r = 0.2\text{mm}$

Theory predicts cross-coupled stiffness at the reduced clearance well.

Theoretical and experimental values converge for the 17% back-pressure 10,200 rpm case of figure 22. The 15,200 rpm case was the last experimental test. The system became unstable and the rotor contacted the seals. This is evident by the widely scattered data. The direct stiffness and direct damping values, however, are not as arbitrary as the cross-coupled stiffness values of figure 22.

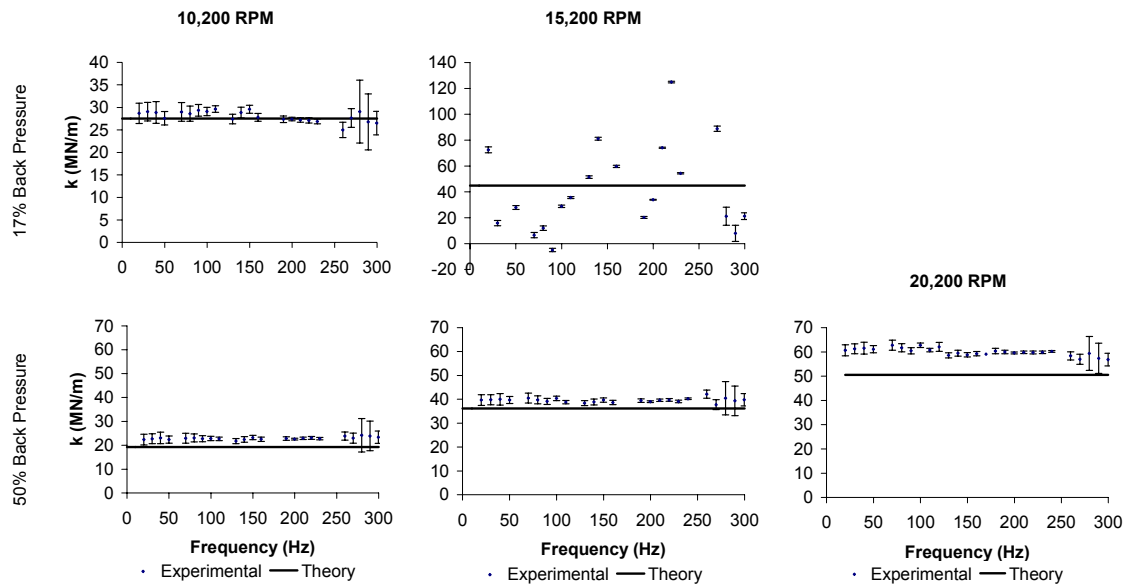


Fig. 22 Experimental and Theoretical Cross-Coupled Stiffness vs. Excitation Frequency, Zero Preswirl, $C_r = 0.1\text{mm}$

Direct Damping

Direct damping is under-predicted by theory in all cases shown in figure 23. Theoretical predictions remain at approximately the same level of under-prediction throughout the different testing configurations. Theory predicts the decrease in direct damping with increasing back-pressure well. Theory predicts a slight frequency dependent nature for the 15,200 rpm and 20,200 rpm 65% back-pressure cases.

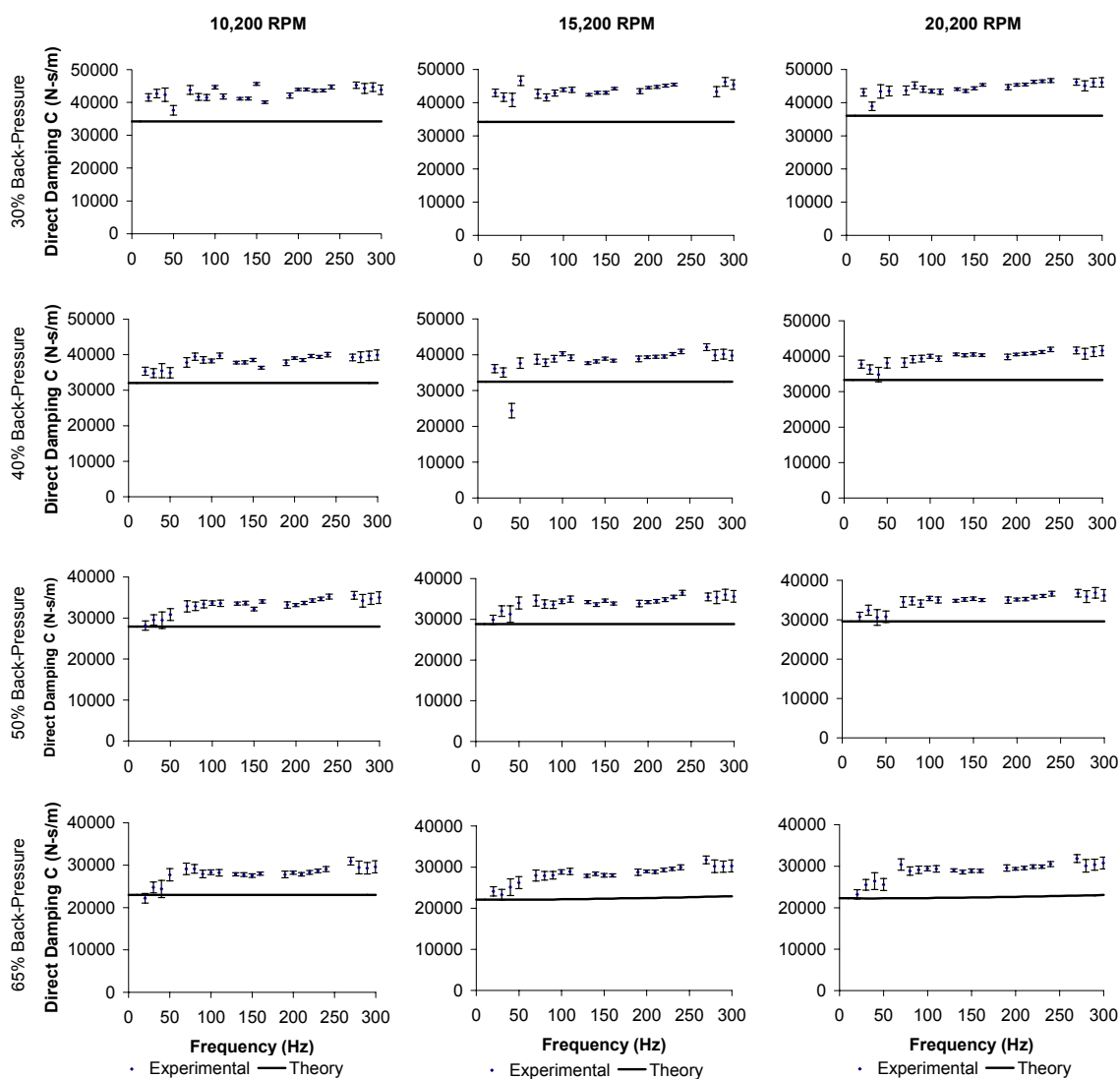


Fig. 23 Experimental and Theoretical Direct Damping vs. Excitation Frequency, Zero Preswirl, $C_r = 0.2\text{mm}$

Direct damping is under-predicted for the medium preswirl 0.2 mm case as shown in figure 24. Experimental and theoretical direct damping change very little with rotor speed or back-pressure. However, theory predicts direct damping at the medium and high preswirl configuration slightly better than the zero preswirl configuration.

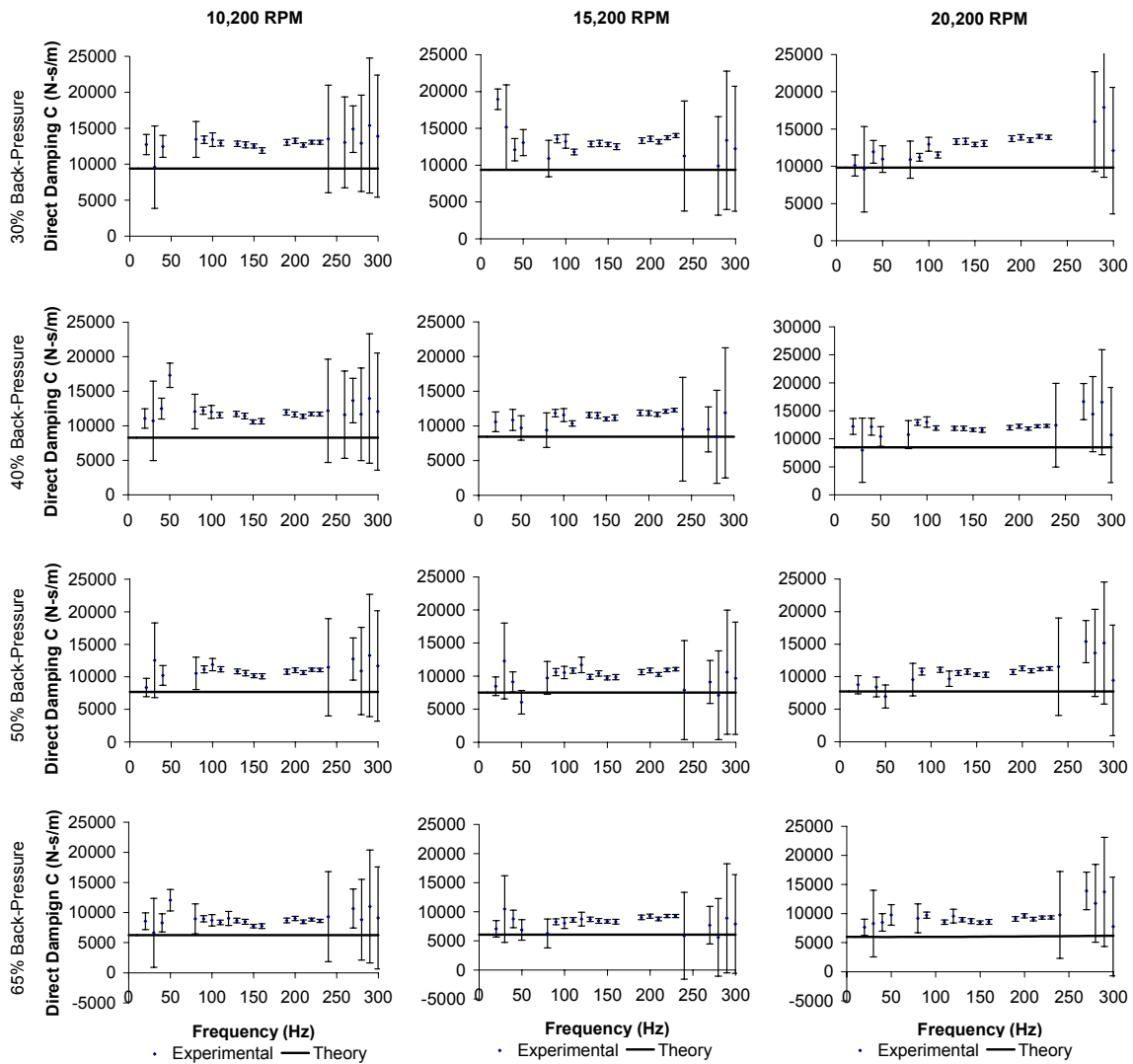


Fig. 24 Experimental and Theoretical Direct Damping vs. Excitation Frequency, Medium Preswirl, $C_r = 0.2\text{mm}$

Theory under-predicts all values of direct damping at the high preswirl 0.2mm clearance as shown in figure 25. Theory predicts a decrease in direct damping with increasing back-pressure. Theory consistently under-predicts direct damping for all levels of preswirl at all rotor speeds and back-pressure ratios.

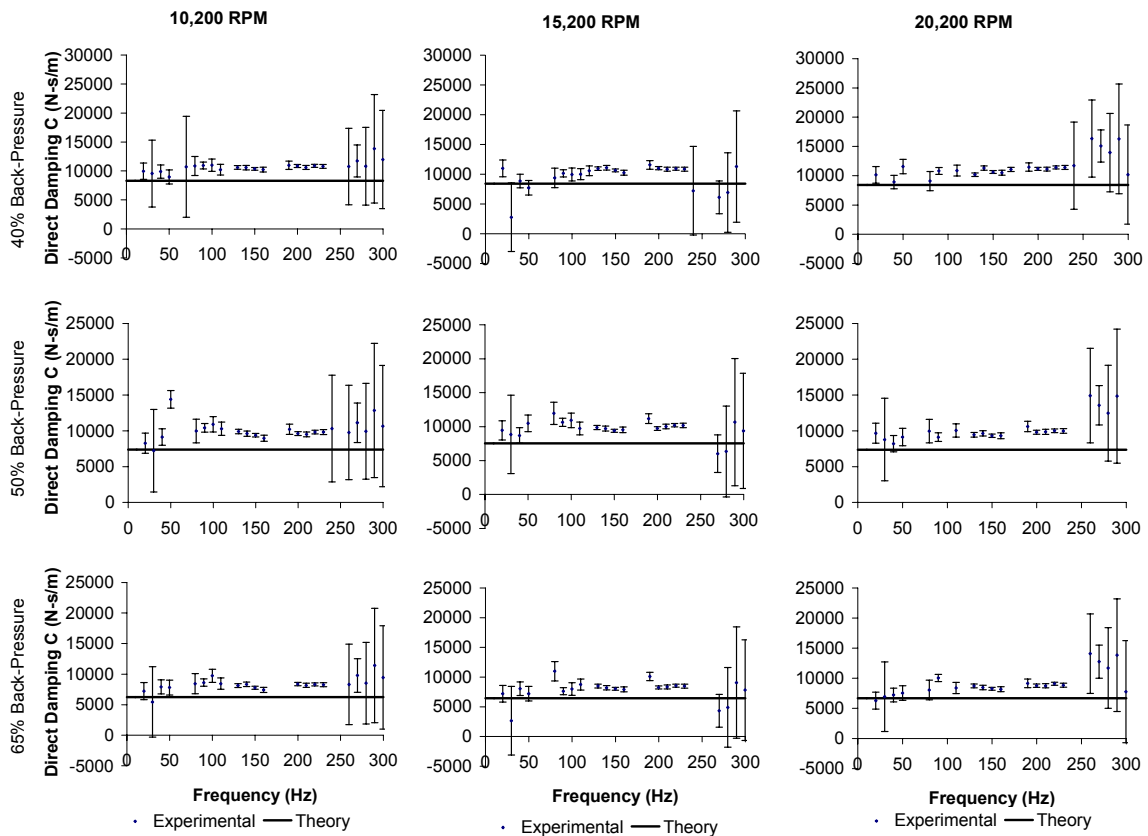


Fig. 25 Experimental and Theoretical Direct Damping vs. Excitation Frequency, High Preswirl, $C_r = 0.2\text{mm}$

Theory under-predicts all experimental values of direct damping at the 0.1 mm operating configuration. Figure 26 shows that experimental direct damping is approximately doubled at the 0.1mm clearance zero preswirl configuration over the direct damping at the zero preswirl 0.2mm clearance configuration. Theory predicts an increase of direct damping with decreasing clearance well. The 15,200 rpm 17% back-pressure graph of figure 26 shows the last case tested. This test resulted in a rub between the test seals and the rotor.

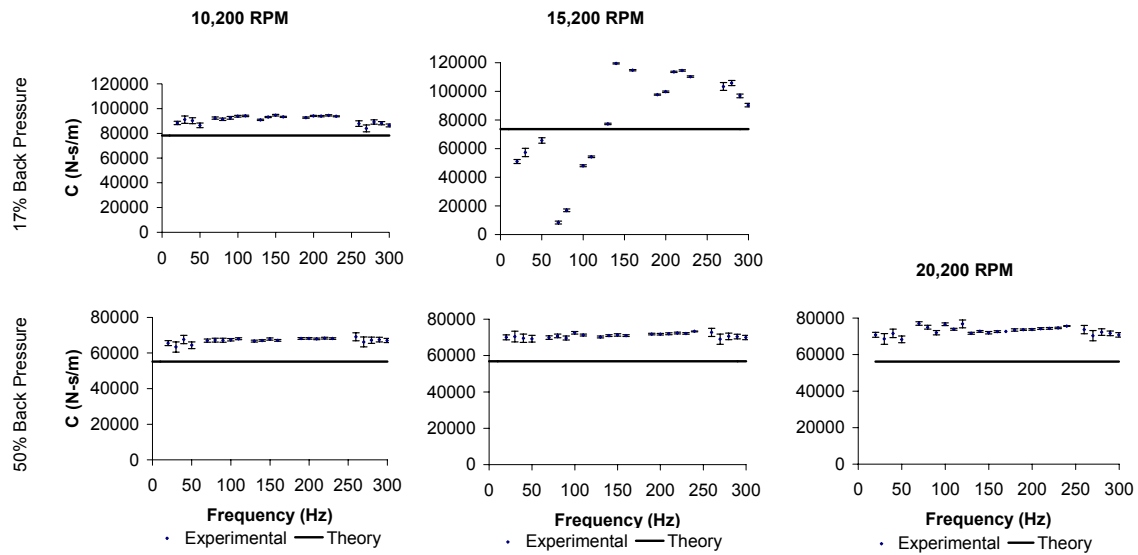


Fig. 26 Experimental and Theoretical Direct Damping vs. Excitation Frequency, Zero Preswirl, $C_r = 0.1\text{mm}$

Effective Stiffness

Effective stiffness closely resembles direct stiffness. The trends discussed in the direct stiffness section of experimental and predicted values hold for effective stiffness. Therefore, no effective stiffness plots are shown.

Effective Damping

The most notable results of figures 27 and 28 are the crossover frequency predictions. Experimental values of effective damping are negative at low excitation frequencies and become positive as the excitation frequency is increased. Theory predicts the crossover frequency well for 30% and 40% back-pressure, zero preswirl configurations. At the 50% and 65% back-pressure ratios, theory predicts a crossover sooner than experimental data shows. The seal is less stable than code predicts at the

50% and 65% back-pressure configurations. The 15,200 rpm and 20,200 rpm, 65% back-pressure are predicted to be frequency dependent. The theory applied for the analysis of the frequency dependent cases is the two-control volume frequency dependent model of Kleynhans [11], all other operating conditions are predicted to be frequency independent. The frequency at which the effective stiffness becomes positive increases with increasing back-pressure and is substantially higher at medium preswirl configurations as can be seen in figure 28.

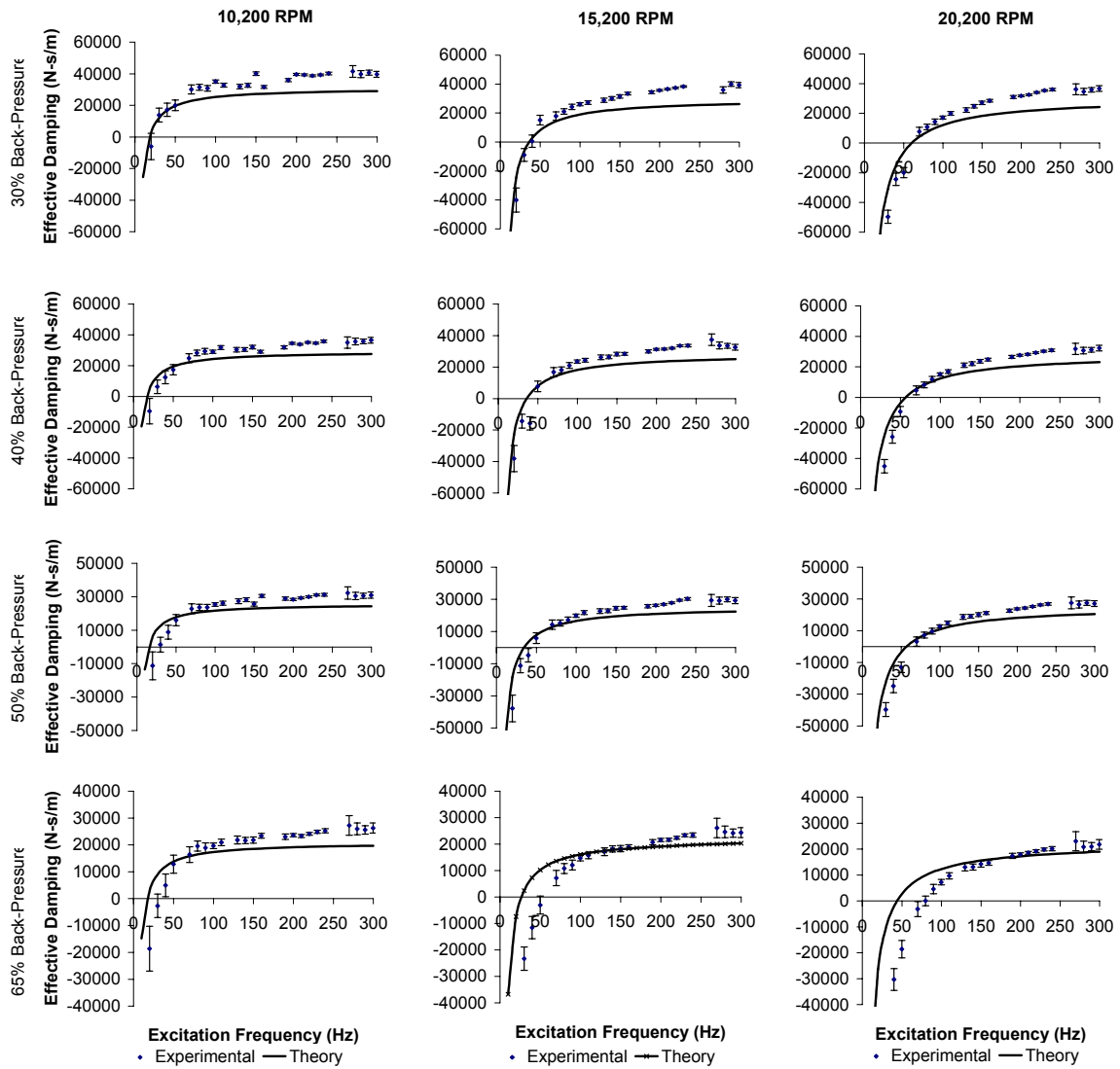


Fig. 27 Experimental and Theoretical Effective Damping vs. Excitation Frequency, Zero Preswirl, $C_r = 0.2\text{mm}$

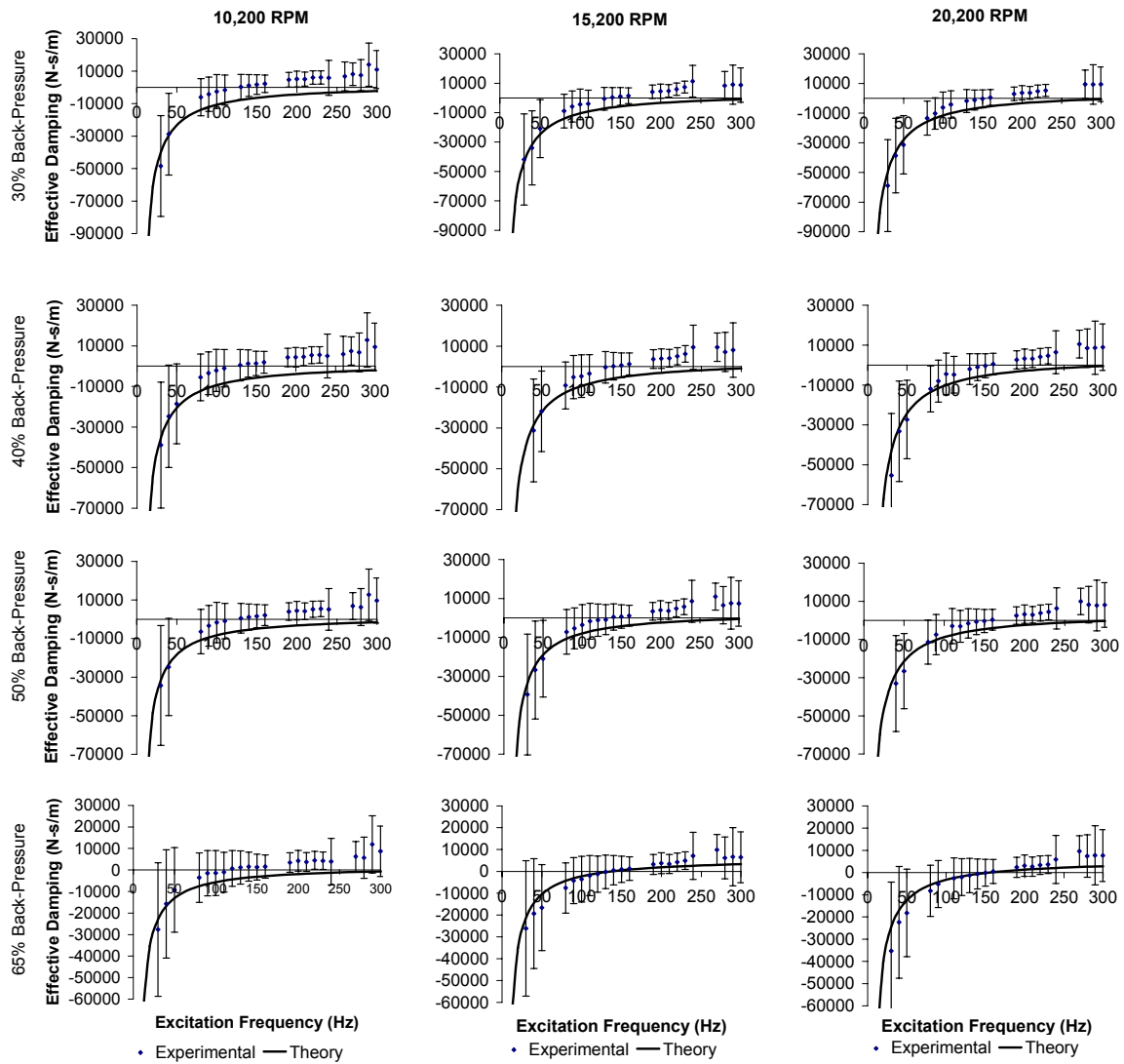


Fig. 28 Experimental and Theoretical Effective Damping vs. Excitation Frequency, Medium Preswirl, $C_r = 0.2\text{mm}$

Theory slightly under-predicts effective stiffness and the crossover point for most of the configurations of figures 28 and 29. Figure 29 shows no cases of frequency dependent. The large variance in figures 28 and 29 is a result of the large variance of the cross-coupled stiffness component of effective damping. Theory predicts many of the

cases of figure 28 and all cases of figure 29 to be unstable, i.e. effective damping is always predicted negative over the frequency range tested. The frequency range tested is well below the test rig natural frequency.

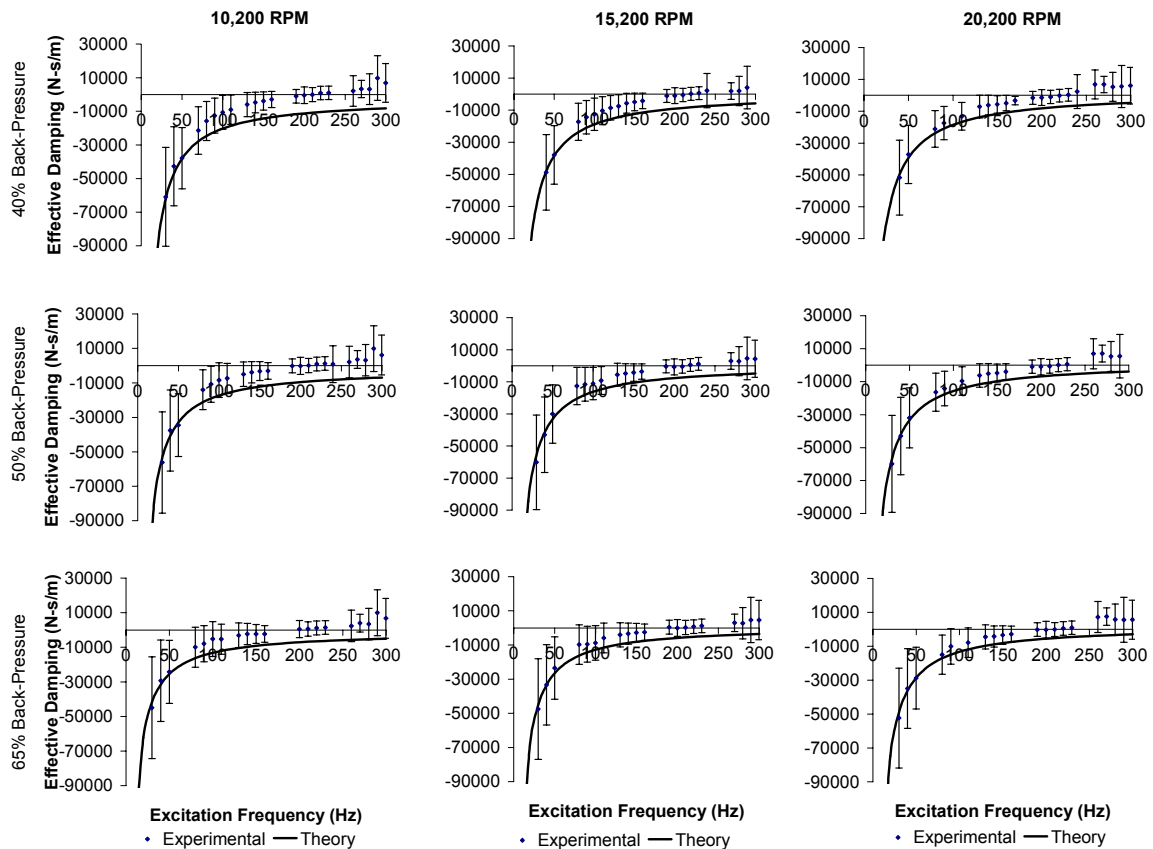


Fig. 29 Experimental and Theoretical Effective Damping vs. Excitation Frequency, High Preswirl, $C_r = 0.2\text{mm}$

Theory under-predicts effective damping and over-predict crossover frequency of the reduced clearance 0.1mm configuration of figure 30. No frequency dependent predictions are made by ISOTSEAL. At the 0.1mm clearance, theory predicts an

increase in effective damping at the 50% back-pressure configuration of figure 30 as compared to the 50% pack pressure configuration of figure 27.

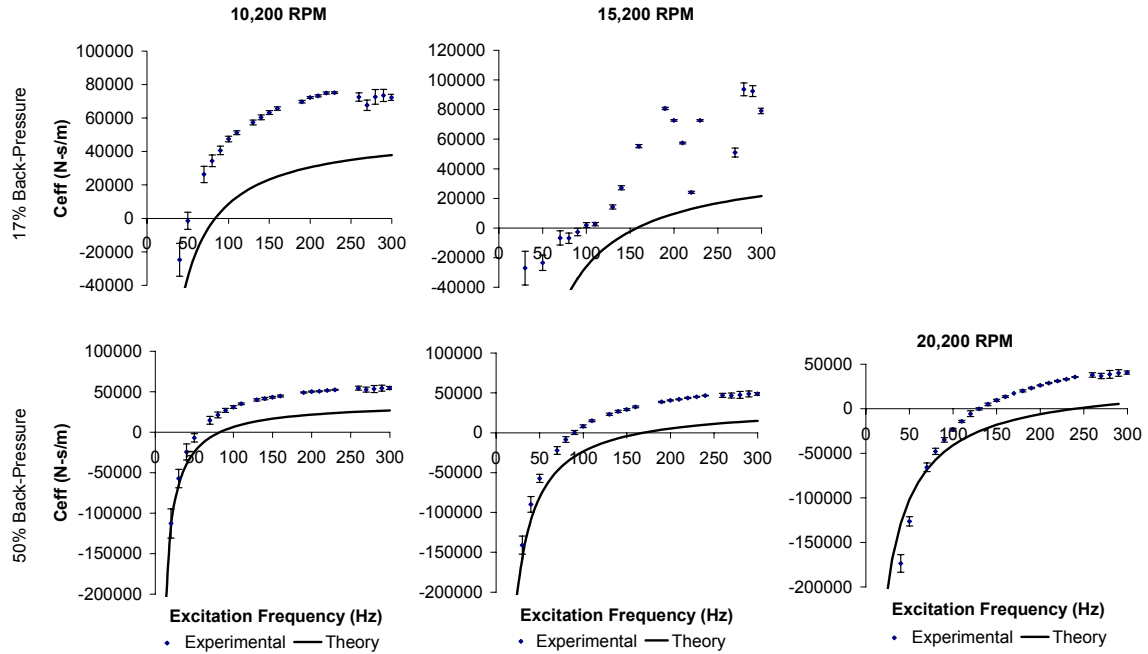


Fig. 30 Experimental and Theoretical Effective Damping vs. Excitation Frequency, Zero Preswirl, $C_r = 0.1\text{mm}$

Seal Leakage

The leakage rates have been non-dimensionalized using equation (15) from Sprowl [14].

$$\phi = \frac{\dot{m}}{\pi \cdot D_s \cdot C_r} \sqrt{\frac{R_c \cdot T_{in}}{2 \cdot P_{in} \cdot \Delta P}} \quad (15)$$

Non-dimensional flow coefficients versus non-dimensional preswirl ratio from equation (3) are shown in figure 31. The flow rates have been non-dimensionalized to compensate for the differences in inlet pressures experienced during testing. Values for

the 0.2mm configurations only are shown. Since values for only one preswirl were obtained at the reduced clearance, flow characteristics cannot be plotted. Theory consistently over-predicts leakage in all cases. Although no graphs are presented for the 0.1mm clearance case, the small number of points available are also consistently over-predicted for all cases. Theory predicts that all 30% back-pressure cases will have choked flow. Figure 31 falsely indicates a decrease in non-dimensional leakage with increasing preswirl. This decrease in leakage is due to the decrease in inlet pressure not an increase in preswirl.

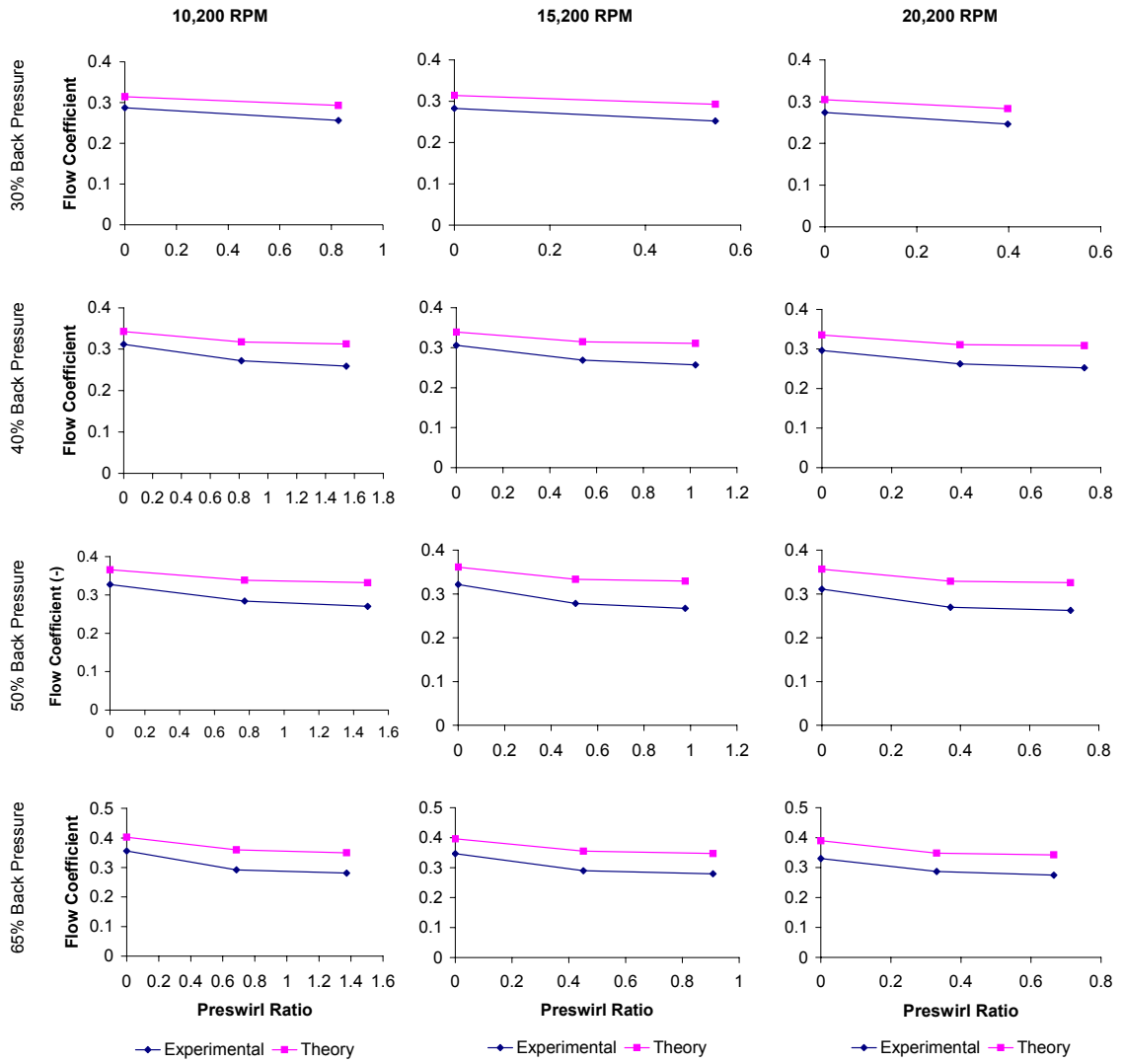


Fig. 31 Experimental and Theoretical Leakage vs. Preswirl Ratio, $C_r = 0.2\text{mm}$

SUMMARY

The objective of this research was to test a set of straight smooth annular gas seals and compare experimental rotordynamic coefficients with predictions of ISOTSEAL. The testing matrix is comprised of multiple pressure drops, rotor speeds, clearances, and fluid preswirls. Parameter influence on rotordynamic coefficients have been investigated.

The desired test could not be completed due to instabilities. Radial stiffeners were added and the inlet pressure was decreased so that the pressure drop across the seals would not induce forces that would cause the system to become unstable. Experimental results show that smooth seals produce undesirable characteristics. The characteristics of smooth seals are of interest since many new seal applications are using honeycomb or hole pattern seals that may become clogged. As the geometric features become clogged, the seals will begin to lose their desired rotordynamic characteristics and behave more like smooth seals. This possibility leads to the conclusion that swirl brakes should be employed in annular gas seal applications in order to disrupt the swirling fluid and decrease the effects of cross-coupled stiffness on the system. The primary interest is direct damping and cross-coupled stiffness, two components of a tangential follower force that drives instability. Cross-coupled stiffness of the smooth seals causes effective damping to remain negative for a wide range of excitation frequencies. The crossover point of effective damping is of great interest for stability prediction. Cross-coupled stiffness increases at medium and high preswirl such that

effective damping remains negative throughout the entire excitation frequency range or becomes positive only at very high excitation frequencies.

Cross-coupled damping is negligible compared to the other coefficients. However, the added mass terms or the direct inertia is not negligible. Approaching an acoustic resonance within the seal has a significant effect on the seals, particularly direct stiffness. The effect is strong enough that the smooth seals begin to exhibit frequency dependent characteristics at high back-pressures.

Experimental values are compared with predictions of ISOTSEAL. Direct stiffness is poorly predicted. Direct damping and cross-coupled stiffness are both under-predicted; however, the predicted values are reasonably close. Effective damping is over-predicted by theory at zero preswirl and crossover frequency is under-predicted. Theory under-predicts direct damping and over-predicts crossover frequency at medium and high preswirl. This results in a more stable seal being predicted than is actually experienced. The few configurations predicted by ISOTSEAL to be frequency dependent are only weakly dependent on excitation frequency. Leakage is consistently under-predicted for all operating conditions.

REFERENCES

- [1] Fleming, D. P., 1977, "High Stiffness Seals for Rotor Critical Speed Control," ASME Paper 77-DET-10, Design Engineering Technical Conference, Chicago.
- [2] Fleming, D. P., 1979, "Stiffness of Straight and Tapered Annular Gas Path Seals," ASME Journal of Lubrication Technology, **101**, No. 3, pp. 349-355.
- [3] Fleming, D. P. 1980, "Damping in Ring Seals for Compressible Fluids," Rotordynamic Instability Problems of High Performance Turbomachinery, NASA CP No. 2133, *Proceedings of a workshop held at Texas A&M University*, pp. 169-188.
- [4] Nelson, C. C., 1984, "Analysis for Leakage and Rotordynamic Coefficients of Surface Roughened Tapered Annular Gas Seals," ASME Journal of Engineering for Gas Turbines and Power, **106**, pp. 927-934.
- [5] Nelson, C. C., 1985, "Rotordynamic Coefficients for Compressible Flow in Tapered Annular Seals," Journal of Tribology, **107**, pp. 318-325.
- [6] Childs, D. W., 1983, "Dynamic Analysis of Turbulent Annular Seals based on Hirs' Lubrication Equations," ASME Journal of Lubrication Technology, **105**, pp. 429-436.
- [7] Childs, D. W., 1983, "Finite-Length Solutions for Rotordynamic Coefficients of Turbulent Annular Seals," ASME Journal of Lubrication Technology, **105**, pp. 437-444.
- [8] Hirs, G. G., 1953, "A Bulk-Flow Theory for Turbulence in Lubricant Films," ASME Journal of Lubrication Technology, **95**, pp. 137-146.
- [9] Nelson, C. C., Childs, D. W., Nicks, C., Elrod, D., 1986, "Theory versus Experiment for the Rotordynamic Coefficients of Annular Gas Seals: Part 2 – Constant-Clearance and Convergent Tapered Geometry," ASME Journal of Tribology, **108**, pp. 433-438.
- [10] Kleynhans, G. F., 1991, "A Comparison of Experimental Results and Theoretical Predictions for the Rotordynamic and Leakage Characteristics of Short ($L/D = 1/6$) Honeycomb and Smooth Annular Pressure Seals," TRC-SEAL-12-91 #384, Turbomachinery Laboratory Report, Texas A&M University.

- [11] Kleynhans, G. F., 1996, "A Two-Control-Volume Bulk-Flow Rotordynamic Analysis for Smooth-Rotor/Honeycomb-Stator Gas Annular Seals," Ph. D. dissertation, Department of Mechanical Engineering, Texas A&M University.
- [12] Kleynhans, G. F., Childs, D., 1996, "The Acoustic Influence of Cell Depth on the Rotordynamic Characteristics of Smooth-Rotor/Honeycomb-Stator Annular Gas Seals," ASME Journal of Engineering for Gas Turbines and Power, **119**, pp. 949-957.
- [13] Weatherwax, M., 2001, "A Study of the Effects of Eccentricity on Honeycomb Annular Gas Seals," M.S. thesis, Department of Mechanical Engineering, Texas A&M University.
- [14] Sprowl, T., 2003, "A Study of the Effects of Inlet Preswirl on the Dynamic Coefficients of a Straight-Bore Honeycomb Gas Damper Seal," M.S. thesis, Department of Mechanical Engineering, Texas A&M University.
- [15] Childs, D., Hale, K., 1994, "A Test Apparatus and Facility to Identify the Rotordynamic Coefficients of High-Speed Hydrostatic Bearings," ASME Journal of Tribology, **116**, pp. 337-344.
- [16] Dawson, P. D., Childs, D. W., Holt, C. G., Phillips, S. G., 2002, "Measurement Versus Predictions for the Dynamic Impedance of Annular Gas Seals: Part 1 – Test Facility and Apparatus," ASME Journal of Engineering for Gas Turbines and Power, **124**, Issue 4, pp. 958-962.
- [17] Childs, D. *Turbomachinery Rotordynamics – Phenomena, Modeling, and Analysis*, John Wiley and Sons, New York, 1993.
- [18] Kurtin, K. A., Childs, D. W., San Andres, L. A., Hale, R. K., 1993, "Experimental Versus Theoretical Characteristics of a High-Speed Hybrid (Combination Hydrostatic and Hydrodynamic) Bearing," ASME Journal of Tribology, **115**, pp. 160-169.
- [19] Dawson, M. P., Childs, D. W., 2002, "Measurement Versus Predictions for the Dynamic Impedance of Annular Gas Seals: Part 2 – Smooth and Honeycomb Geometries," ASME Journal of Engineering for Gas Turbines and Power, **124**, Issue 4, pp. 963-970.
- [20] Ha, T. W., Childs, D. W., 1992, "Friction-Factor Data for Flat-Plat Tests of Smooth and Honeycomb Surfaces," ASME Journal of Tribology, **114**, pp. 722-730.

APPENDIX A

SAMPLE BASELINE DATA

Table 1A Baseline Data

f	rz11	iz11	rz12	iz12	rz21	iz21	rz22	iz22
20	1.224	0.315	-0.084	-0.003	-0.267	-0.048	1.329	0.282
30	1.294	0.462	-0.188	-0.005	-0.335	-0.048	1.529	0.358
40	0.992	1.031	-0.281	-0.055	0.089	-0.205	1.403	0.596
50	1.069	0.684	-0.140	-0.113	-0.248	-0.039	0.949	0.864
60	1.332	0.941	0.810	1.387	-0.387	-0.012	1.057	1.400
70	1.248	0.762	0.057	0.159	-0.307	-0.080	1.328	0.505
80	1.181	0.779	-0.017	0.137	-0.264	-0.131	1.266	0.770
90	1.165	0.902	-0.219	0.210	-0.329	-0.083	1.375	0.919
100	1.199	0.966	-0.205	0.258	-0.249	-0.087	1.325	1.033
110	1.160	1.161	-0.227	0.456	-0.211	-0.159	1.316	1.110
120	1.176	1.312	-0.127	0.546	-0.267	0.072	1.402	1.196
130	1.388	1.438	-0.209	0.571	-0.273	-0.214	1.528	1.501
140	1.194	1.634	-0.114	0.914	-0.114	-0.115	1.483	1.295
150	1.260	1.713	0.188	1.063	-0.050	-0.240	1.351	1.504
160	1.041	1.926	0.384	1.144	-0.100	-0.234	1.425	1.533
170	1.371	2.096	0.792	1.005	0.068	-0.507	1.437	1.735
180	1.245	1.480	1.118	1.015	0.407	-0.340	1.154	2.268
190	1.915	3.378	1.164	0.780	-0.121	-0.994	1.139	2.277
200	1.953	2.211	0.596	0.557	-0.452	-0.696	1.801	2.358
210	1.372	2.823	0.502	0.746	0.095	-1.095	1.835	2.588
220	1.714	2.911	0.571	0.561	-0.428	-1.527	1.714	2.783
230	1.613	3.369	0.482	0.555	-0.645	-1.961	1.820	3.090
240	1.859	3.742	0.815	0.477	-0.618	-2.269	2.149	3.254
250	6.605	7.318	-29.821	-36.340	-1.028	-9.745	-20.935	61.796
260	2.971	4.642	-1.362	2.888	-2.927	-2.468	6.502	2.769
270	2.146	4.686	-0.870	0.602	-1.270	-1.291	4.597	2.477
280	1.963	5.059	0.109	1.295	-0.629	-2.133	2.052	1.429
290	1.721	5.895	0.447	1.043	-1.020	-2.501	1.557	3.425
300	2.304	6.740	0.615	0.464	-1.007	-3.469	1.926	3.879

Table 1A shows a sample of the baseline impedance data with no radial stiffeners. The data is shown in 10 Hz intervals and can be transformed to coefficients

by equation 7. In tables 1A and 2A, r_z and i_z indicate the real and imaginary part of the impedance respectively, and 1 and 2 indicate the x and y directions respectively. Table 2A is a sample of the baseline data with the radial stiffeners employed. The increase in direct and cross-coupled stiffness in the baseline data is explained with a simplified model in figure 1A below.

Table 2A Baseline Data with Radial Stiffeners

f	r_{z11}	i_{z11}	r_{z12}	i_{z12}	r_{z21}	i_{z21}	r_{z22}	i_{z22}
20	5.496	0.088	-4.015	-0.020	-4.146	-0.012	5.450	0.029
30	5.463	0.104	-3.947	0.001	-4.088	-0.038	5.438	0.145
40	5.492	0.163	-4.063	0.042	-4.209	-0.026	5.504	0.151
50	5.380	0.191	-4.038	0.114	-4.194	0.003	5.456	0.225
60	5.251	0.767	-4.372	0.599	-4.329	-0.010	5.070	0.305
70	5.427	0.498	-3.930	0.193	-4.005	-0.026	5.320	0.271
80	5.393	0.322	-3.985	0.128	-4.038	0.011	5.514	0.294
90	5.302	0.380	-4.018	0.248	-4.058	-0.053	5.337	0.297
100	5.191	0.496	-3.913	0.344	-3.912	-0.098	5.246	0.415
110	5.453	0.736	-4.180	0.296	-4.139	-0.195	5.437	0.567
120	5.287	0.807	-4.030	0.560	-3.947	-0.134	5.150	0.743
130	5.351	0.793	-3.952	0.804	-3.947	-0.172	5.325	0.622
140	5.134	0.952	-3.599	0.969	-3.768	-0.172	5.096	0.663
150	5.160	1.285	-3.138	0.802	-3.577	-0.456	4.898	1.035
160	5.643	1.627	-3.543	0.594	-3.989	-0.776	5.593	1.417
170	5.739	1.280	-2.969	0.893	-3.844	-0.612	5.845	0.959
180	5.913	2.427	-2.641	1.717	-4.518	-0.533	4.671	1.108
190	5.578	2.142	-2.405	0.620	-3.785	-1.121	4.992	1.235
200	5.617	1.478	-3.061	0.156	-3.946	-0.805	5.511	1.666
210	6.582	2.067	-2.930	0.146	-3.594	-0.855	5.459	1.588
220	5.607	1.733	-2.678	0.550	-3.687	-1.307	5.424	1.700
230	5.487	2.306	-2.518	0.330	-3.978	-1.590	5.478	2.053
240	5.057	10.848	10.497	-5.857	-5.632	-8.931	-8.264	6.490
250	5.848	0.120	-0.256	-5.662	-9.914	-0.084	0.734	9.759
260	8.037	1.395	0.834	-7.797	-4.731	-0.921	-0.354	4.865
270	11.390	10.876	11.570	-12.301	-5.546	-7.830	-8.533	6.196
280	11.661	5.449	5.614	-14.036	-9.088	-6.353	-7.549	11.416
290	20.580	-7.486	-7.759	-19.753	-14.802	2.939	3.376	14.378
300	12.966	3.821	0.191	-16.660	-10.089	1.298	3.095	9.927

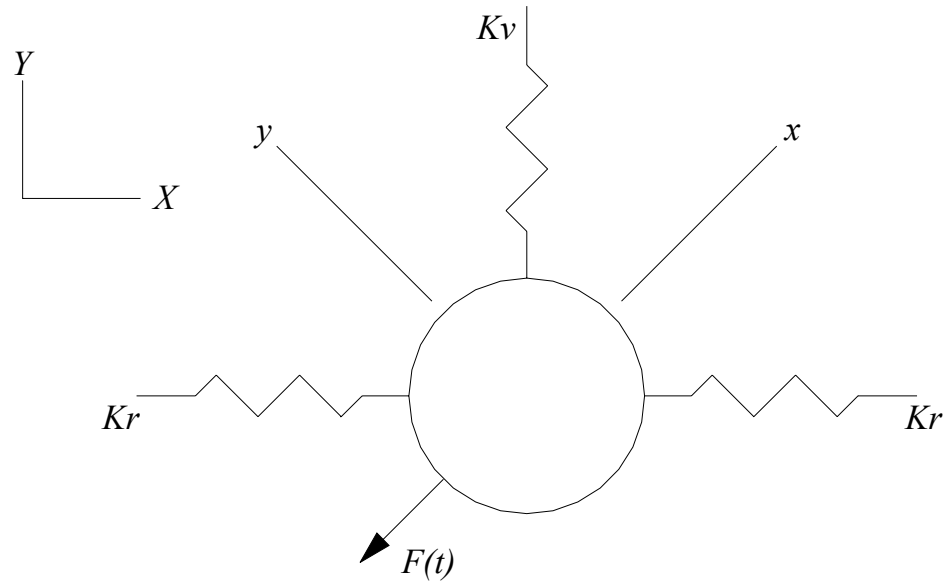


Fig. 1A Stator Model with Radial Stiffeners

In figure 1A, the radial stiffness Kr is much greater than the vertical stiffness Kv .

The following equations will transform the stiffness values from the X - Y coordinate system to the x - y coordinate system.

$$\begin{Bmatrix} F_x \\ F_y \end{Bmatrix} = \begin{bmatrix} Kr & 0 \\ 0 & Kv \end{bmatrix} \begin{Bmatrix} X \\ Y \end{Bmatrix} \quad (1A)$$

Force in the X - Y coordinate system is given by equation 1A. The X - Y coordinate system is transformed to the x - y coordinate system via a rotation matrix R in equation 2A. The rotation matrix R is given in equation 3A. The X - Y force is transformed into the x - y coordinate system by equation 4A.

$$\begin{Bmatrix} x \\ y \end{Bmatrix} = \begin{bmatrix} \cos \frac{\pi}{4} & \sin \frac{\pi}{4} \\ -\sin \frac{\pi}{4} & \cos \frac{\pi}{4} \end{bmatrix} \begin{Bmatrix} X \\ Y \end{Bmatrix} \quad (2A)$$

$$R = \begin{bmatrix} \cos \frac{\pi}{4} & \sin \frac{\pi}{4} \\ -\sin \frac{\pi}{4} & \cos \frac{\pi}{4} \end{bmatrix} \quad (3A)$$

$$\begin{Bmatrix} F_x \\ F_y \end{Bmatrix} = R \begin{Bmatrix} F_X \\ F_Y \end{Bmatrix} \quad (4A)$$

Equations 2A and 4A are rearranged and substituted into equation 1A yielding equation 5A. The new stiffness K' in the x - y coordinate system is found using equation 6A. After simplification K' is found as equation 7A.

$$R^{-1} \begin{Bmatrix} F_x \\ F_y \end{Bmatrix} = \begin{bmatrix} K_r & 0 \\ 0 & K_y \end{bmatrix} R^{-1} \begin{Bmatrix} x \\ y \end{Bmatrix} \quad (5A)$$

$$\underline{K}' = R \underline{K} R^{-1} \quad (6A)$$

$$\underline{K}' = \frac{1}{2} \begin{bmatrix} K_r + K_y & K_y - K_r \\ K_y - K_r & K_r + K_y \end{bmatrix} \quad (7A)$$

Equation 7A yields large values for the cross-coupled terms, the off diagonal terms of equation 7A that have the same sign. This is consistent with the sample baseline data shown in table 2A.

APPENDIX B

INSTRUMENTATION

The test apparatus is capable of controlling six independent parameters: fluid supply and exit pressure, rotor speed, static position, excitation amplitude, and excitation frequency. Data sampling and recording capabilities are supplied by a Hewlett Packard 3852A multi-channel data acquisition and control unit (12-bit A/D; resolution at +/- 10 VDC range = 4.88 mV; accuracy = 0.1% of reading + 5 mV) system linked to a Pentium-computer via an IEEE-488 interface. A C-language program is used to direct the data manipulating tasks. Instrumentation of the test section allows for the measurement of air pressure, temperature, and leakage flow-rate. Also measured are relative motion between the rotor and stator, acceleration, and dynamic excitation forces. Detailed specifications for each of the transducers and readouts (power, units, etc.) used to obtain corresponding test data measurements are presented below.

Fluid pressure measurements:

Kulite Semi-Conductor XTM-190-1000SG and 2000SG miniature piezoresistive pressure transducers with 10 VDC excitation; 1.15 mV/bar (0.078 mV/psi) and 0.56 mV/bar (0.038 mV/psi) sensitivity; < +/- 3% FSO zero pressure output (residual unbalance); +/- 1% FSO max. combined non-linearity, hysteresis, and repeatability. Calibrated with dead-weight tester and daily shunt calibrated to approximate calibration factors of 6.12 bar/Volt (90 psi/Volt) and 12.2 bar/Volt (180 psi/Volt). Custom in-house op-amps output +/- 10 VDC to HP A/D system or are manually recorded.

Temperature measurements:

Type K thermocouples; 2.2 °C (4.0°F) or 0.75% max. error, calibrated with Omega portable hand-held calibrator and/or ice bath and boiling water to approximate calibration factors of 55.6 °C/Volt (100 °F/Volt). Readout and power unit was an Omega DP 30 temperature indicator with 0.05 °C (0.1 °F) resolution, analog output with linearity of 1 mV/count and accuracy of +/- 2 mV. Values were output to the HP A/D system or manually recorded from readouts.

Motion of the test stator relative to the rotor (excitation amplitudes):

Bently Nevada 330601 Proximity Probes with 3300 REBAM Transducer System; 0 to 10 kHz frequency response, 0.0394 V/ μ m (1 V/mil) sensitivity, <= 4 mV noise floor, 0.254 micrometer (10 μ -inch) measurement ability. Originally calibrated with Mitutoyo electronic digital micrometers with 1.27 μ m (50 μ -inch) resolution using a linear regression least-squares curve fit to obtain approximate calibration factors of 25.4 μ m/Volt (1.0 mil/Volt). Daily shunt calibration is performed.

Output of 0 to -20 VDC output converted with custom in-house op-amps to +/- 10 VDC. Values were output to the HP A/D system.

Acceleration of the test stator:

PCB Piezotronics model 307A accelerometers; +/- 50 g max. range, 0.005 g resolution, 2.1% sensitivity, 5 VDC FS. Originally supplied with calibration certificate and proved on TAMU acceleration tester. Approximate calibration factor of 100.2 mV/g. Daily check for offset is performed. Equipped with Brüel and Kjaer UA 0559 mechanical filters to shield high frequency vibration. PCB Piezotronics line powered signal conditioner Model 494A21 power unit; 0.3 Hz low frequency response (-5%), 100 kHz high frequency response (+5%), 150 μ V RMS broadband noise (unity gain). Output to HP A/D system.

Dynamic excitation forces applied to the test stator:

Zonic/Xcite model 2522 load cells with signal conditioner/op amp integral with controller; 11.1 kN (2500 lbs) FS, approximately 1 mV/V FS output, approximate linearity of 0.5% of FS. Originally supplied with manufacturers calibration certificate with approximate calibration factor of 1.1 kN/Volt (250 lbs/Volt), +/- 10 VDC FS. Daily shunt calibration is performed. Output to HP A/D system.

Air leakage through the test article:

Flow Technology, Inc. FM series axial turbine flow-meter, model number FT-16NER2-GEA-1; NIST calibration to +/- 0.5% uncertainty of reading at 95% confidence level. Flow Technology, Inc. RI51 digital flow-rate indicator, model number RI51-1-C-0000-6; 0.5% max. indicator error, 0.5% max output voltage error. Output to HP A/D system or manually recorded.

Mass Flow-Rate Calculation

Mass flow-rates were calculated for the seals at each test condition by converting displayed SCFM (Standard Cubic Feet per Minute) values obtained from a calibrated flow-meter/flow-computer to reasonably correct kg/sec values using the following relationships:

- A recorded SCFM value represented the flow-rate for a pair of seals; hence, the output was divided by a factor of 2 and then by 60 to convert to SCFS (Standard Cubic Feet per Second).
- The SCFS values were then divided by the standard conversion of 35.31466 cubic feet per cubic meter to obtain SCMS (Standard Cubic Meters per Second).

- These SCMS values are based on standard conditions of 1.01 bar-a (14.7 psia) and 26.7 °C (80 °F) at the calibration pressure of (70.0 bar-a) (1015 psia). SCMS values were then converted to ‘uncorrected’ kg/s by multiplying the SCMS values by 1.1778 kg/m³ (This value was obtained from an NIST thermophysical air properties code with the air density at 1.01 bar-a and 26.7 °C).
- To compensate flow-rate values for differences in temperatures measured through the flow-meter during testing versus flow-meter calibration temperatures, the flow-rate values were adjusted by a ratio of absolute temperature [(‘uncorrected’ kg/s) * (calibration temp. + 273)/(test temp. + 273)], as recommended by the flow-meter manufacturer. A suitable calibration temperature of 1.67 °C (35 °F) was used (based on calibration temperatures at measured flow-rates) and test temperatures were measured upstream and downstream of the flow-meter.
- To account for variances in test pressures from the calibration pressure of 70.0 bar, the flow values were then multiplied by the ratio of the actual measured flow-meter test pressure to the calibration pressure of 70.0 bar-a [(‘uncorrected’ kg/s) * (measured pressure in bar-a) / 70.0 bar-a] to obtain ‘corrected’ kg/s mass flow-rates for each seal.

Note: The provided ‘corrected’ mass flow-rate values have many sources of uncertainty. It could be argued that a more accurate method of determining the flow-rates would be to use a ratio of densities at test versus calibration conditions (pressure and temperature). However, there are uncertainties with temperature and pressure measurements and the calibration data does not provide for adequate compensation for varying temperatures or densities.

Flow-Meter Calibration

Mass flow-rate calculations were obtained based on flow-meter/flow-computer calibration data dated February 2002. Based on this calibration data, flow measurements were recorded in SCFM and converted to corresponding mass flow-rate values (kg/s) as described in the previous section.

VITA

Bradley Gray Kerr was born on September 30, 1979, in Jonesboro, Arkansas, United States of America. He was raised in Arkansas, and graduated from Highland High School, in Highland Arkansas, in 1998. In the fall of 1998, he began studies at the University of Arkansas at Fayetteville where he earned his Bachelor of Science in mechanical engineering. In the fall of 2002, he began studies at Texas A&M University where he earned his Master of Science in mechanical engineering in 2004. Bradley plans to continue his studies at Texas A&M University in pursuit of the degree of Doctor of Engineering.

Permanent Address

Bradley G. Kerr
P.O. Box 413
Ash Flat, AR 72513